A Neural Model of Surface Perception: Lightness, Anchoring, and Filling-In

Stephen Grossberg and Simon Hong*

Department of Cognitive and Neural Systems
And
Center for Adaptive Systems
Boston University
677 Beacon Street, Boston, MA 02215, USA

Abbreviated title: A Neural Model of Surface Lightness Perception

Submitted: October 2004
Revised: May 2005

Technical Report CAS/CNS TR-2003-16

All correspondence should be addressed to
Professor Stephen Grossberg
Department of Cognitive and Neural Systems
Boston University
677 Beacon Street
Boston, MA 02215
Phone: 617-353-7858
Fax: 617-353-7755
Email: steve@bu.edu

Keywords: Surface perception, Lightness, Anchoring, Filling-in, Retinal adaptation, Long-range horizontal connections, Visual cortex

* Authorship in alphabetical order. SG and SH were supported in part by the Air Force Office of Scientific Research (AFOSR F49620-01-1-0397), the Defense Advanced Research Projects Agency and the Office of Naval Research (ONR N00014-95-1-0409), the National Science Foundation (NSF SBE-0354378), and the Office of Naval Research (ONR N00014-01-1-0624).

Abstract

A neural model is proposed of how the visual system processes natural images under variable illumination conditions to generate surface lightness percepts. Previous models clarify how the brain can compute relative contrast. The Anchored Filling-In Lightness Model (aFILM) clarifies how the brain "anchors" lightness percepts to determine an absolute lightness scale that uses the full dynamic range of neurons. The model quantitatively simulates lightness anchoring properties (Articulation, Insulation, Configuration, Area Effect) and other lightness data (discounting the illuminant, the double brilliant illusion, lightness constancy and contrast, Mondrian contrast constancy, Craik-O'Brien-Cornsweet illusion). The model clarifies how retinal processing stages achieve light adaptation and spatial contrast adaptation, and how cortical processing stages fill-in surface lightness using long-range horizontal connections that are gated by boundary signals. The new filling-in mechanism runs 1000 times faster than diffusion mechanisms of previous filling-in models.

1. Introduction

1.1 From Luminance to Anchored Lightness. The retina receives luminance signals, which are a product of reflectances and illumination levels (Hurlbert, 1986; Lambert, 1760; Wyszecki & Stiles, 1982), from objects in the world. Surface reflectances, or the percentages of light reflected by a surface in each wavelength (also known as albedo), provide information about the material properties of objects. From these luminance signals, the visual system is able to estimate object reflectances by compensating for an immense dynamic range of mean illuminations across time, and for a wide dynamic range across a single scene. This process of "discounting the illuminant" is not sufficient, however, to efficiently see the world because illuminant-discounted signals may represent only the *relative* amounts of light that each object surface reflects to the eyes. For effective perception, the brain also needs to compute an *absolute* lightness scale that can represent the full-range of experience from dim moonlight to dazzling sunlight.

Early neural models of surface lightness perception simulated many classical psychophysical data based upon estimates of relative light levels, including brightness constancy, contrast, and assimilation; Craik-O'Brien-Cornsweet effect; Koffka-Benussi ring; Kanizsa-Minguzzi anomalous brightness differentiation; Hermann grid; Land Mondrians viewed under constant and gradient illumination conditions that could not be explained by Land's Retinex theory; Bergström brightness percepts of step-like and smoothly modulated luminance profiles; Hamada brightness percepts of luminance increments and decrements; Mach bands; low-contrast and high-contrast missing fundamental and nonlinear contrast effects associated with sinusoidal luminance waves; and Ehrenstein brightness enhancement (Cohen & Grossberg, 1984; Grossberg & Todorovic, 1988; Gove, Grossberg, & Mingolla, 1995; Neumann, Pessoa, and Mingolla, 1998). Consistent extensions of these models simulated 3D figure-ground brightness percepts, such as Fechner's paradox; binocular brightness summation; Bregman-Kanizsa figure-ground separation; Kanizsa stratification; Munker-White effect; Benary cross; checkerboard percepts;

McCollough effect; Necker cube; transparency, and 3D neon color spreading (Grossberg, Hwang, & Mingolla, 2002; Grossberg & Kelly, 1999; Grossberg & Swaminathan, 2004; Grossberg & Yazdanbakhsh, 2003, 2004; Kelly & Grossberg, 2000; ((Ross & Pessoa, 2000))).

Given the large amount of already simulated data, the present article developed a model that is consistent with these earlier explanations, while also proposing how an absolute lightness scale may be constructed by the brain. To realize this goal, the new Anchored Filling-In Lightness Model (aFILM) provides a more sophisticated account of early visual filtering, lightness filling-in, and lightness anchoring. The model quantitatively simulates, for the first time, key psychophysical data about lightness anchoring, as well as other lightness data to show that it is consistent with earlier model explanations. Neurophysiological and anatomical data that support model hypotheses are also summarized; see Table 1. aFILM can also process complex natural scenes under difficult lighting conditions. Although the present work focuses on achromatic images, a variant of the model has been shown capable of processing chromatic natural images as well (Hong & Grossberg, 2004). The model was briefly reported in Hong & Grossberg (2003).

1.2 Discounting the Illuminant by Early Visual Preprocessing. Retinal preprocessing of visual signals contributes to discounting the illuminant and creating a relative lightness scale. These processes include two mechanisms of gain control: *Light adaptation* and *contrast adaptation*. Human vision adapts to ten orders of magnitude of daily variations of ambient illumination (Cornsweet, 1970; Dahai & Spitzer,

Table 1

Anatomy, Experiments	*Functional interpretation (equations in model)*	*Selected references (species)*
Outer segment of retinal photoreceptor	Automatic gain control (A1-A3)	Koutalos & Yau (1996, frog, salamander, cow, human)
Inner segment of retinal photoreceptor and HC connection	Shift property by negative feedback (A4-A5)	Verweij et al. (1996, goldfish)
HC syncytium	Input dependent gated diffusion (A6-A8)	Kamermans et al. (1996, goldfish)
Retinal ganglion cells, LGN cells; Physiology of ON, OFF channels.	Center-surround property of ON, OFF channels (A9-A24)	Jones et al. (2000, cat), Rosck et al. (2000, tiger salamander); Schiller (1992, frog, mudpuppy, goldfish, rabbit, cat, monkey)
V1 simple cells	Polarity-dependent boundary detection (A25-A32)	Alonso et al. (2001, cat), Hubel & Wiesel (1962, cat)
V1 complex cells	Polarity-independent boundary detection (A33-A35)	Alonso & Martinez (1998, cat)
Filling-in related cortical activities in V1, V2; Psychophysics of filling-in	Boundary-gated filling-in (A36-A44)	Hung et al. (2001, cat); Paradiso and Nakayama (1991, human)
Lightness perception	Anchoring of lightness (A45-A53)	Gilchrist et al. (1999, human)

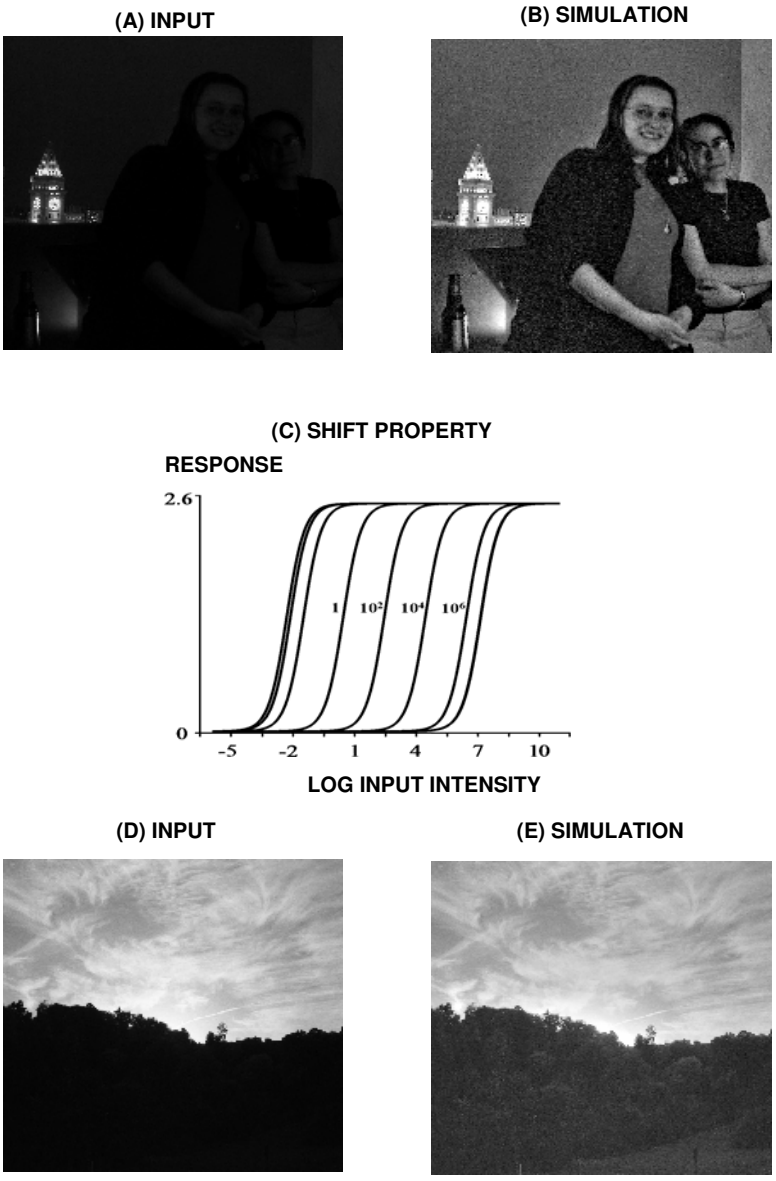

Figure 1. Retinal adaptation. (A-B) Input and the simulation of the model reflecting the result of light adaptation of the retina. (C) Shift property of sensitivity of the model retinal units. The model retina simulates the light adaptation property by automatically shifting its operating range to adapt to the ambient luminance of the visual field. When the luminance is too low, it simulates the physical limit of adaptation (the saturation of shifting on the left end of the graph). For clarity only four mean input intensities are shown besides the corresponding curves. The visible 3 leftmost curves have mean luminances of 10^{-4}, $10^{-3,}$ and 10^{-2} from the left-end, respectively. The visible rightmost curve has a mean luminance of 10^{7}. (D-E) Input with high spatial contrast and the model simulation of the input. It is assumed that the retinal circuit is responsible for this kind of non-linear rescaling of contrast that makes the brain "see" the dark part as well as the bright part. Photo courtesy of Arash Fazl and Bob Wagner.

1996; Kaufman, 1974; Martin, 1983; Sakmannn & Creutzfeldt, 1969). For example, if the brain gets an input like the one in Figure 1A, we "see" it as in Figure 1B. This *light adaptation* property depends in part on retinal circuitry. Figure 1C shows the model response to varying background illumination. The range of maximal sensitivity shifts with background illumination without undergoing compression, as also occurs in the retina (Rodieck, 1998; Werblin, 1971). Another dimension of adaptation is spatial *contrast adaptation*. For example, if there is a big contrast in the visual field, as in Figure 1D, the brain can rescale input signals to see the dark side as well as the bright side of the scene, as in the model simulation of Figure 1E. Since retinal ganglion cells, which are the sole output units of the retina, have firing rates that vary over less than three orders of magnitude, the visual system needs to compress the dynamic range of input at the retinal level, without a loss of sensitivity. Mechanisms of contrast

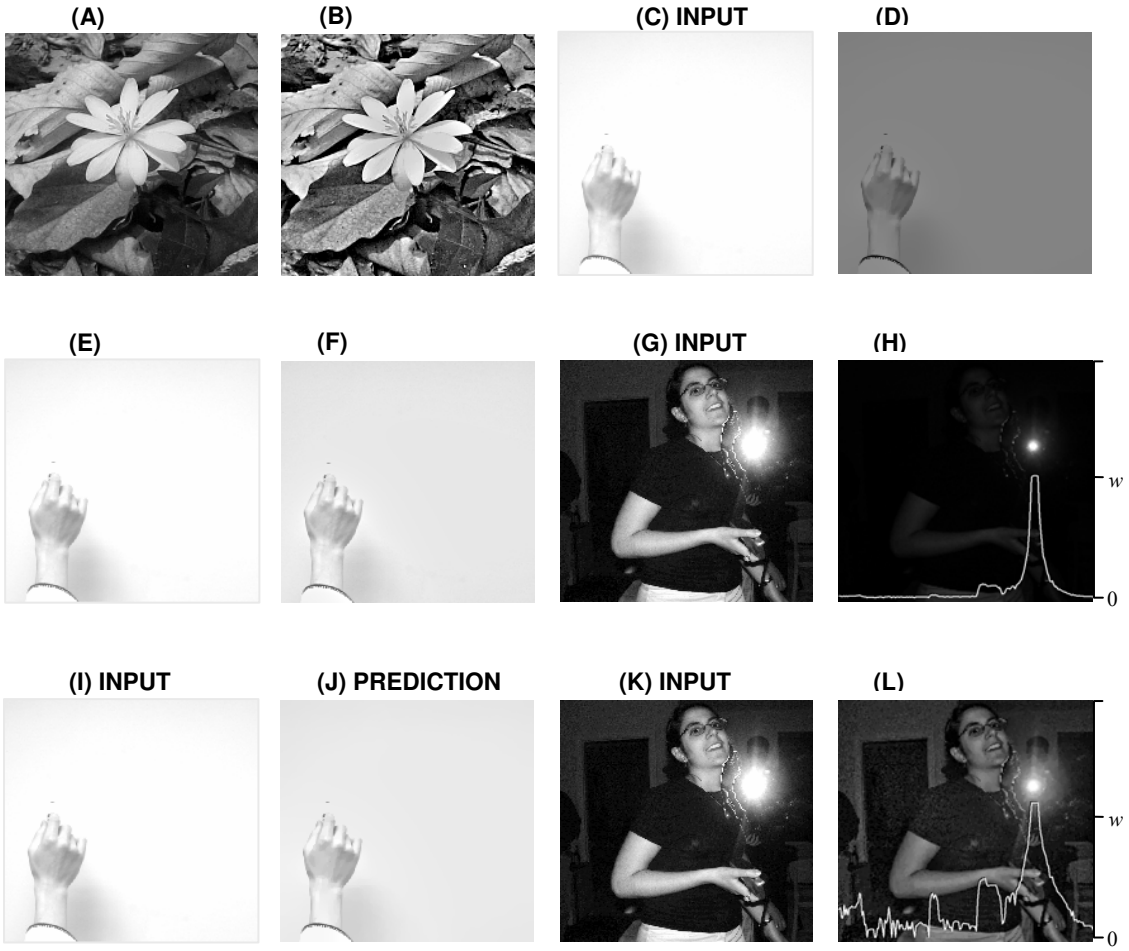

Figure 2. Predictions by various lightness theories. (A-B) Input and correct prediction of lightness by *average luminance rule*. (C-D) Input and wrong prediction by *average luminance rule*. According to *average luminance rule*, the whiteboard should look middle gray. (E-F) Input and correct prediction of lightness by *Highest-luminance-as-white* (HLAW) rule. (G-H) Example where HLAW rule makes an error. HLAW rule makes an error due to a prominent highest luminance like the one in (G). (I-L) Inputs and corresponding predictions made by the model developed here. The model with a new rule called *blurred-highest-contrast-as-white* (BHCAW) rule correctly predicts percepts. See the text for further explanations.

adaptation are still undergoing intensive experimental study (Demb, 2002; Baccus & Meister, 2002). Some retinal gain control mechanisms contributing to adaptation include: (1) Ca^{2+} ion-mediated negative feedback at the photoreceptors (Koutalos & Yau, 1996) and bipolar cells (Nawy, 2000); (2) bleaching of photopigments (Dowling, 1987; Fain, 2001); (3) surround negative feedback by horizontal cells (HC) (McMahon et al., 2001; Thibos & Werblin 1978; Werblin, 1974); and (4) a circuitry switch from cones to rods (Mills & Massey, 1995; Ribelayga, Wang & Mangel, 2002).

1.3 Some Anchoring Hypotheses. Surface lightness percepts cannot fully be explained by such low-level mechanisms. For starters, visual percepts depend upon appropriate interactions between both ON and

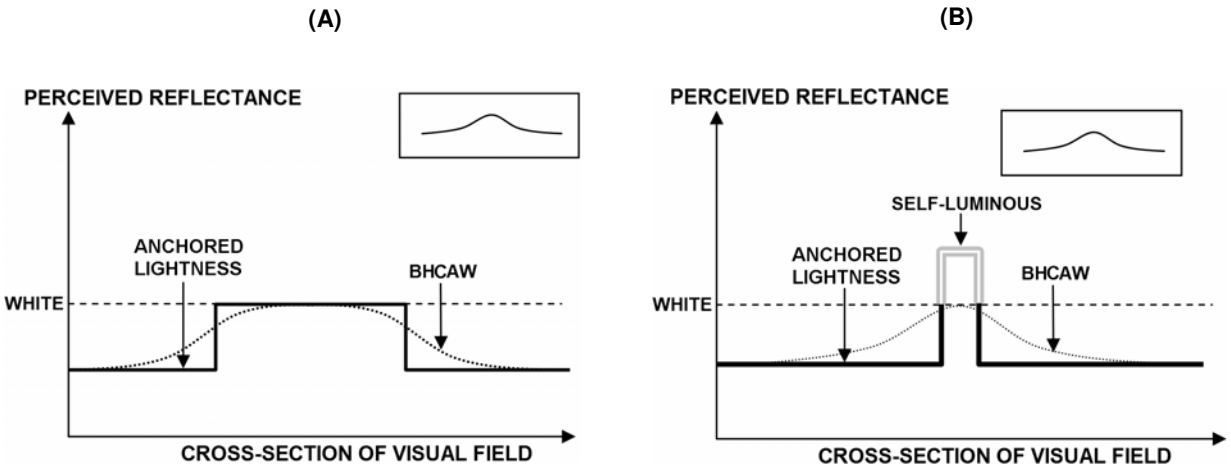

Figure 3. *Blurred-highest-contrast-as-white* (BHCAW) rule and spatial scale. (A) BHCAW rule with a large area of highest luminance. The dashed line indicates the value of WHITE which the blurred highest luminance attains. The thick line (ANCHORED LIGHTNESS) illustrates a 1-D profile of the anchored lightness. In this example, the blurred highest luminance equals white because the area of the highest luminance is at least as large as the kernel used for blurring in the BHCAW module (the inset). (B) BHCAW rule with a small area of highest luminance. Here the blurred highest luminance is smaller than the highest luminance because of the small size of the area of highest luminance relative to the blurring kernel. When the blurred highest luminance is anchored at white, the highest luminance gets pushed above white, becoming self-luminous.

OFF channel signals that are largely segregated up until cortical area V1 (Schiller, Sandell & Maunsell, 1986; Schiller, 1992). Attempts to explain surface lightness range from the classic *inference* theory of Helmholtz (1866) to recent theories that Gilchrist and his colleagues classify as *intrinsic image* theories (Arend 1994; Gilchrist et. al., 1999). Several theories propose that lightness is derived from luminance ratios among surfaces in a display, but these computations can only recover relative lightness values. There remains the problem of mapping relative lightness values to the absolute lightness values that are experienced. One proposed solution is the *average luminance rule* of Helson (1943), which postulates that the average luminance of the display, defined as middle gray, is an "anchor" for other luminances; higher luminances than average luminance will then have higher lightness values than middle gray. Figures 2A and 2B show an example where this rule makes a correct prediction. However, in response to Figure 2C, it make((s)) the error shown in Figure 2D: The whiteboard becomes middle gray. The *average luminance rule* thus does not explain lightness data quantitatively. Wallach introduced an anchoring hypothesis which became known as *highest-luminance-as-white* (HLAW) rule (Horn 1977; Land & McCann, 1971; Wallach, 1948, 1976). This rule assumes that the perceptual quantity "white" is assigned to the highest luminance in a given scene as the standard, and that lower luminant surfaces are assigned to gray values relative to it. According to this rule, the whiteboard in Figure 2E should look white, as in Figure 2F. In cases like Figure 2G, however, the HLAW rule makes a wrong prediction, as shown in Figure 2H. The white curve in Figure 2H that is superimposed on the image shows the profile of the predicted lightness along the horizontal section of the image that crosses the light source. The value "*w*" in Figure 2H marks

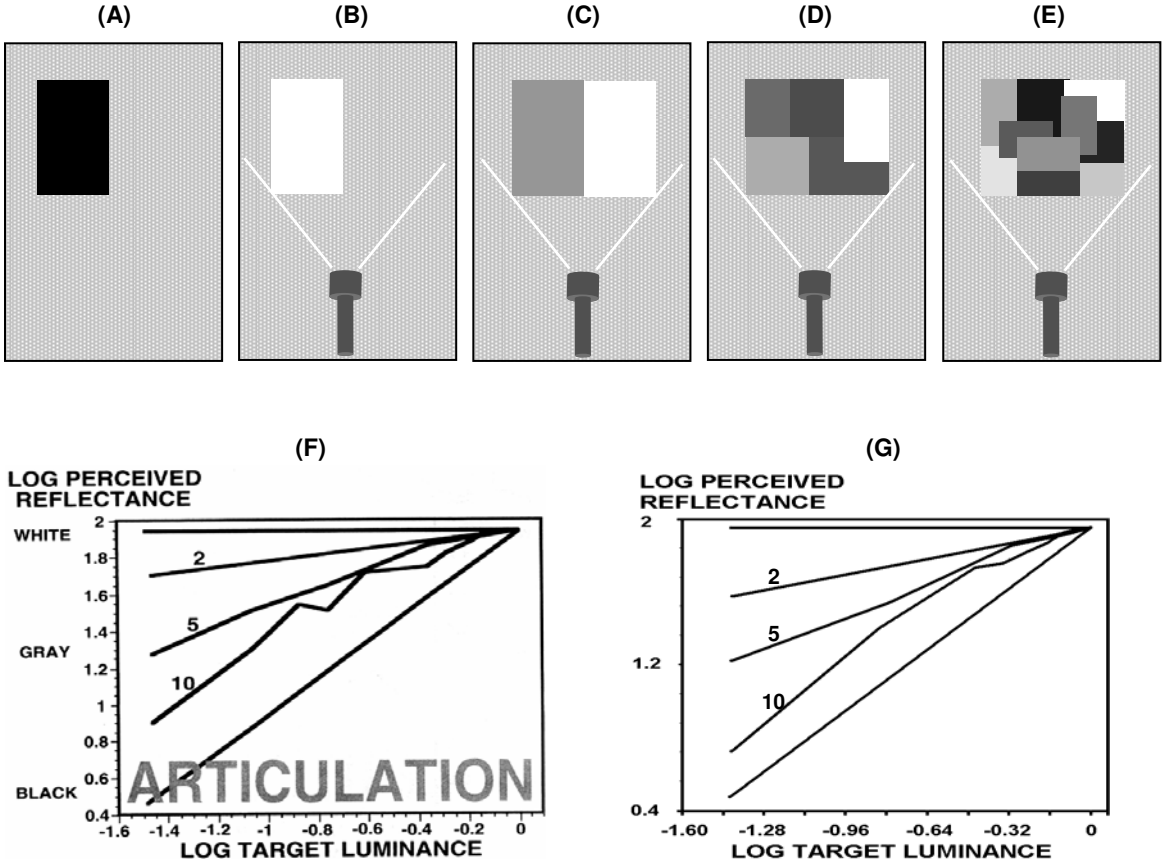

Figure 4. Articulation effect. (A-E) Illustration of the procedure and percepts of Articulation effect experiment. See the text for details. The patterned backgrounds illustrate the dark background in the experiment. (F) Data of Articulation effect. As more gray patches are added to a display, the range of perceived reflectance (lightness) widens. In the graph, the widening of the perceived reflectance corresponds to the steeper overall curve as the number of gray level target surfaces increases from one to ten as illustrated in B to E. The widening effect makes the gray patches look darker. The diagonal line shows the perfect situation of lightness constancy. The horizontal line shows the situation where there is just one surface on the Ganzfeld (a homogeneous background covering the entire visual field with no other visual cues). (G) Simulation results. PERCEIVED REFLECTANCE in the model is ANCHORED LIGHTNESS of the simulation. See the text for details. Figure F is from Gilchrist et al. (1999).

the lightness value "white" along the vertical axis. By converting the intense illumination source into "white," the HLAW rule drives other lightness values to dark levels.

To overcome these shortcomings, the current model proposes how brain dynamics may instantiate a new anchoring rule called the *blurred-highest-contrast-as-white* (BHCAW) rule. Blurring, or spatial integration, is sensitive to the area subtended by the highest luminance, thus introducing spatial scale into the lightness computation (Figure 3A). Blurring also predicts why some surface regions appear self-luminous (Figure 3B). See Section 2.5 for further explanation.

Figures 2I and 2J show a model simulation that provides a result like the HLAW rule in Figures 2E and 2F. Figures 2K and 2L, in contrast, show how the BHCAW rule can correctly predict lightness when a

bright light source occurs, which was not done by HLAW. The curve on Figure 2L shows the simulated lightness profile of the image horizontal section that crosses the light source. The peak of the curve going above white "*w*" predicts that the light source will look self-luminous. The model can also quantitatively simulate the four sets of data (Articulation, Configuration, Insulation, and Area Effect) that Gilchrist and his colleagues (1999) have proposed should be explained by any quantitative lightness theory, as is shown next.

Articulation Effect. Figures 4A to 4E illustrate the procedure and the percepts of the Articulation Effect: A black patch (reflectance 3%) is fixed in front of a homogenous dark background (Figure 4A). When the patch gets illumination 30 times that of the dark background resulting in the luminance of 1.4 ftL (foot Lambert), it looks white (Figure 4B). (This 30-to-1 foreground-background illumination setting is also used in the Configuration, Insulation, and Area Effect). When a real white patch (reflectance 90%) appears near the white-looking black patch, the black patch appears gray (Figure 4C). In the experiment, the subjects indicated perceived reflectance by selecting a match from a Munsell chart of 16 examples. The Munsell chart was illuminated with a different light source so that the luminance of the whitest white, Munsell 9.5, was 160 ftL. That a black surface can look white when intensely illuminated, as illustrated in Figure 4B, is called the Gelb effect (see Cataliotti & Gilchrist, 1995). As more gray patches are added, the less luminant ones ones look increasingly dark (Figures 4C, D and E). This darkening effect does not affect the highest luminance surface, which remains "anchored" to white (Figure 4F). Figure 4G shows the that the model can quantitatively simulate these data. (No effort was made to show error bars in the simulations since none appeared with the data.) Even in the two-Mondrian case in Figure 4C, the reflectances of the patches range from black to white covering the full span of reflectance used in the experiment. Adding different luminance patches is thus just a process of "articulation".

Configuration Effect. Figures 5A and 5B illustrate the procedure and the percepts of the Configuration Effect: A Mondrian display in Figure 5B—namely, a 2-D arrangement of juxtaposed gray patches—widens the range of perceived reflectance compared to the linear arrangement of patches shown in Figure 5A. That is, the dark patches in Figure 5A appear lighter than the corresponding dark patches in Figure 5B. Figures 5C and 5D show the data. Comparison of the 5C and 5D shows that this effect becomes greater with more local articulation. Figures 5E and 5F show that the model can quantitatively simulate this effect.

Insulation Effect. Figures 6A to 6C show the procedure and the percepts of the Insulation Effect: When the staircase arrangement is surrounded by a white insulating region, the range of perceived reflectance widens (Figure 6B). This does not occur when the staircase is insulated by a black border (Figure 6C). Figure 6D summarizes the data and Figure 6E the simulation.

Area Effect. The lower part of Figure 7A shows the Area Effect set-up. The subject's head is covered by a dome that is divided into two regions. The upper part of Figure 7A illustrates the stimuli and corresponding percepts. When the highest luminance area occupies more than half of the visual field, it appears white while the darker part looks gray. As the darker area occupies more than half of the visual

field, it approaches white, while the lighter area appears self-luminous. Figure 7B shows the data and Figure 7C the model simulation.

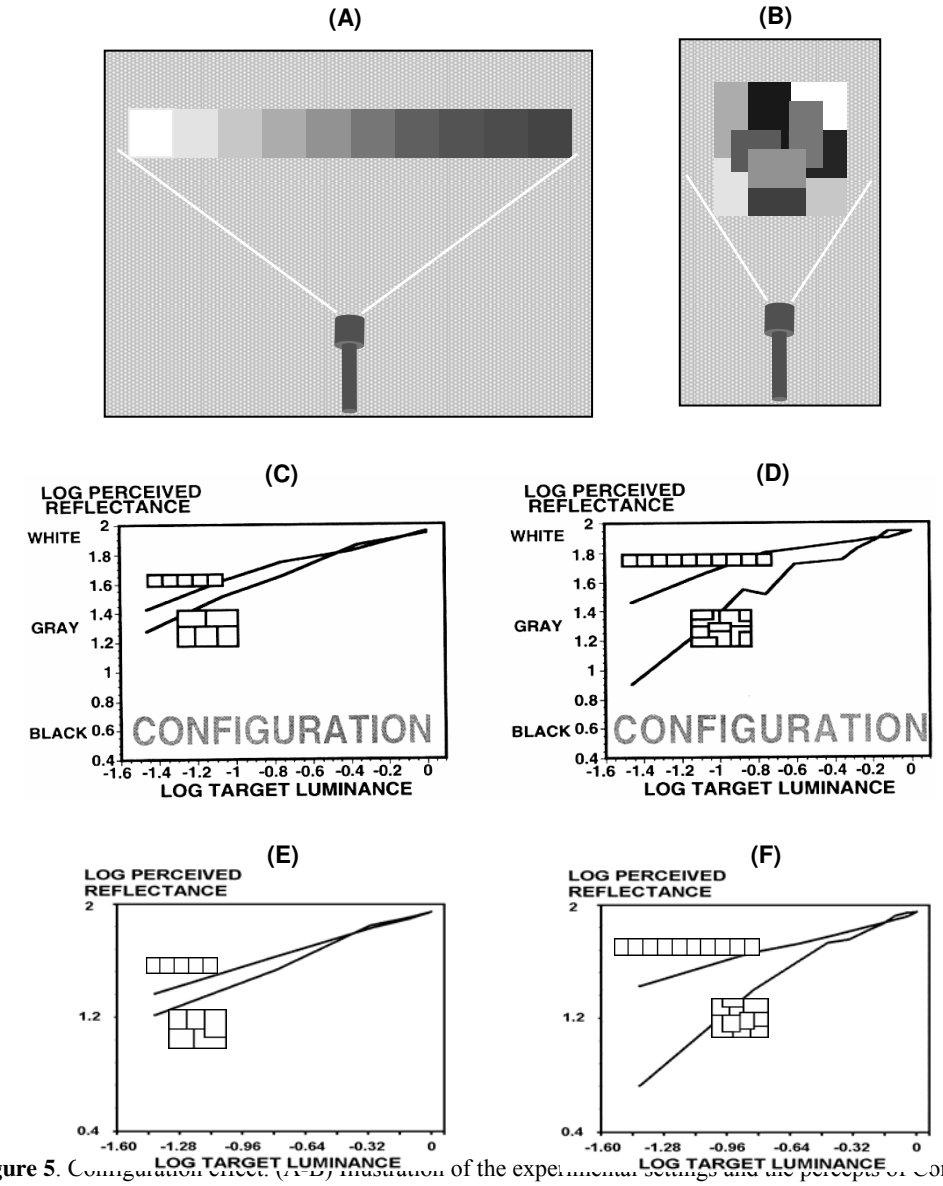

Figure 5. Configuration effect. (A-B) Illustration of the experimental settings and the percepts of Configuration effect. See the text for details. (C-D) Data of Configuration effect. The lower inset of each figure shows the Mondrian arrangement; the upper inset, staircase arrangement. Mondrian arrangement of gray target surfaces widens the range of lightness compared to the staircase arrangement. Comparison of C and D shows that articulation makes the effect bigger. (E-F)

No published models have yet simulated these data using an anchoring process, among other stages in processing lightness information. Below it is explained how the aFILM simulates these and other lightness data. The reader who prefers can skip to the Results Section 3 for model simulation explanations before reading about the model in Section 2.

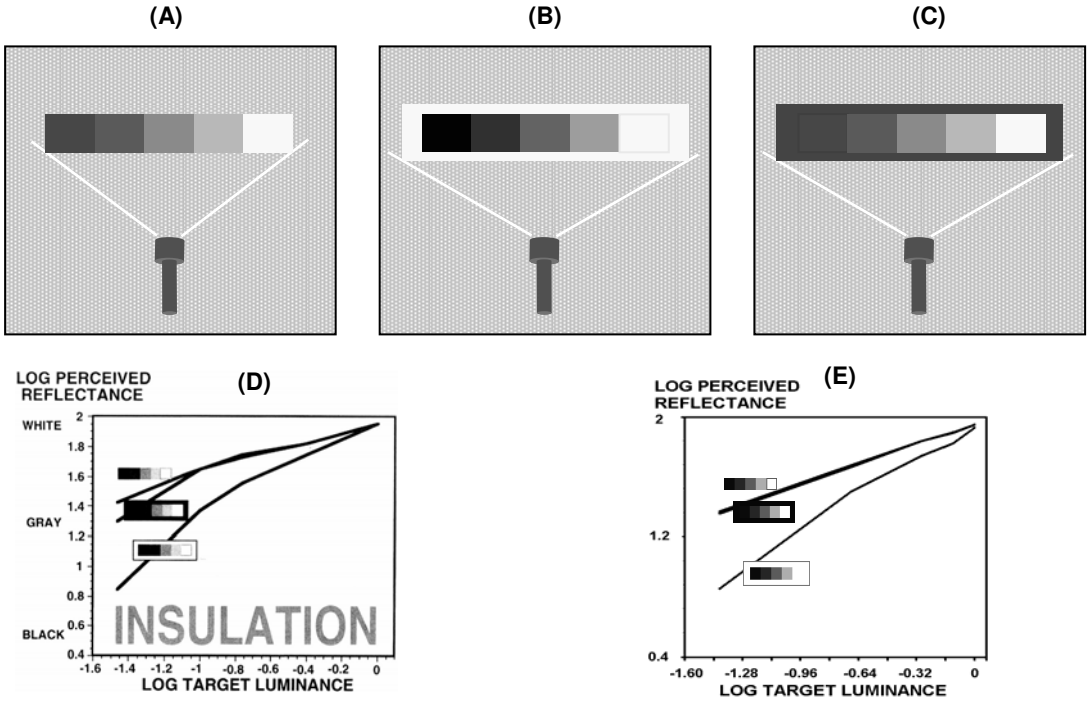

Figure 6. Insulation effect. (A-C) Illustration of the experimental settings and the percepts of Insulation effect. See the text for details. (D) Data of Insulation effect. Insulation by a white surrounding widens the range of perceived reflectance. This effect does not seem to happen when a black surrounding is used for insulation. (E) Simulation results. The model fits the data of configuration effect in the anchoring theory. See the text for further explanation. Figure D is from Gilchrist et al. (1999).

Figure 7. Area effect in divided Ganzfeld situation. (A) Illustration of the experimental settings and the percepts of Area effect. See the text for details. (B) Qualitative illustration of the area effect. As the non-highest luminance area becomes bigger than the half of the visual field, it approach to white, while the smaller area of highest luminance becomes luminous. The divided discs along the abscissa with light and dark surfaces show the configurations of the stimuli. (C) Simulation result of Area effect. The model simulates the concept of the effect quantitatively. The squares along the abscissa with light and dark surfaces show the configurations of the stimuli. See the text for details. Figure B is from Gilchrist et al. (1999).

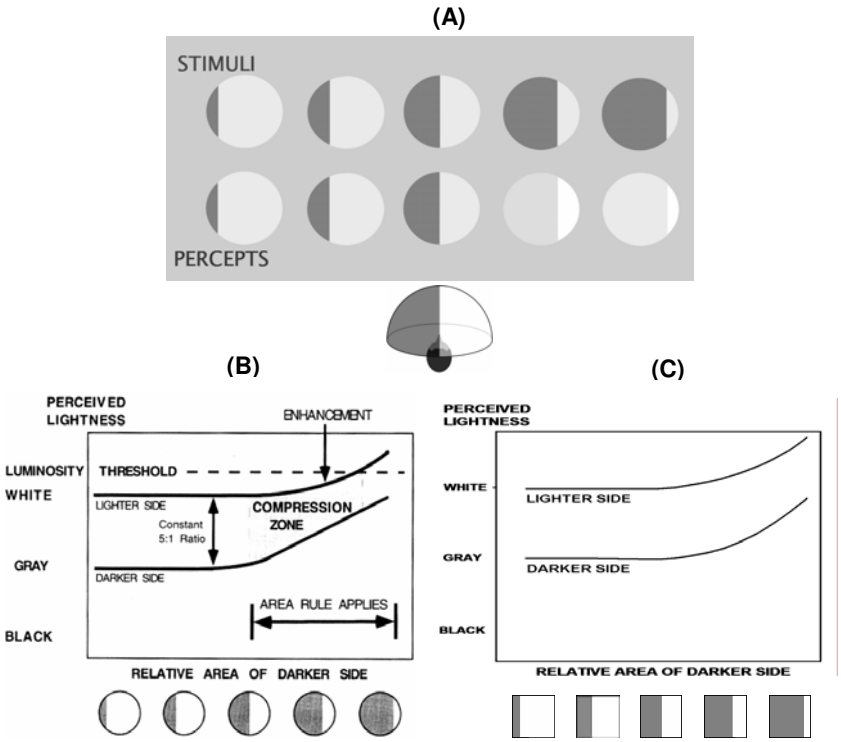

2. Model Description

Figure 8 provides a model macrocircuit. Variants of its processing stages, except the Anchored Lightness and BHCAW stages, have earlier been used to simulate lightness data. The present model refines the operations in these stages as well, as indicated below. The Retinal Adaptation stage adapts to ambient luminance and spatial contrasts. Using the adapted signal, the Contrast stage generates contrast signals using multiple-scales of antagonistic ON-center OFF-surround and OFF-center ON-surround processes. The light-adapted signal also goes without change via a parallel pathway to the Luminance stage. The model then branches into two cortical streams, the boundary and surface streams, which have previously been modeled as a Boundary Contour System (BCS) and Feature Contour System (FCS), respectively (Grossberg, 1994, 1997; Grossberg & Kelly, 1999; Grossberg & Mingolla, 1985a, 1985b; Grossberg & Howe, 2003; Grossberg & Swaminathan, 2004; Grossberg & Todorovic, 1988; Kelly & Grossberg, 2000). The luminance and contrast signals are pooled at the Surface Filling-In stage, where their spread via long-range horizontal connections is gated, or blocked, by contrast-sensitive signals from the Boundary stage. The filled-in signals are then rescaled at the Anchored Lightness stage. These anchored signals represent perceived lightness in the model.

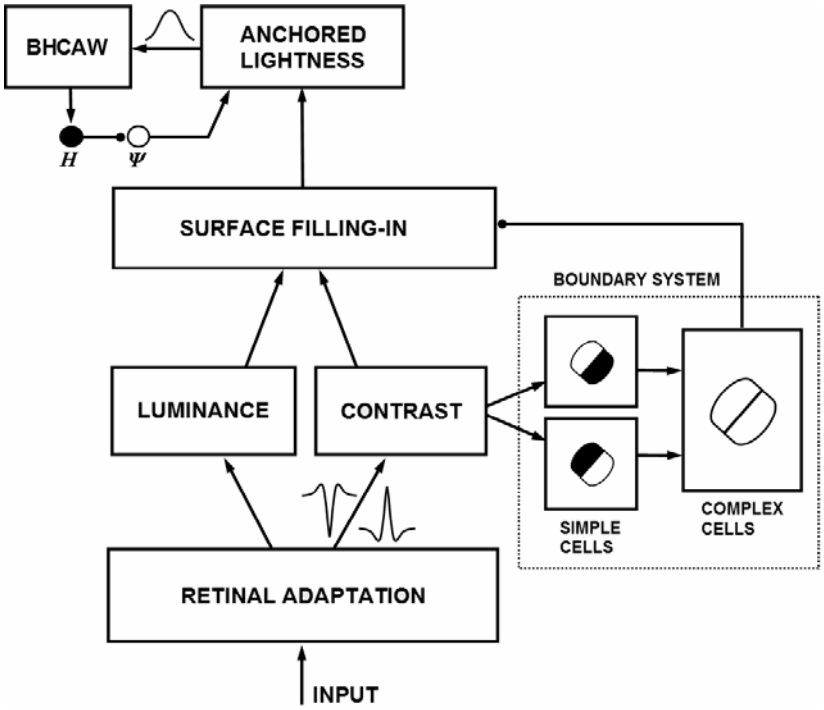

Figure 8. Illustration of the model. See the text for details. Each box indicates an array of cells doing a similar task. Arrow-heads indicate excitatory signals for the post-synaptic units; round-heads indicate inhibitory. The Mexican-hat shape and the up-side-down shape of it between the RETINAL ADAPTATION and CONTRAST modules illustrate the one-dimensional shapes of the on-center off-surround and off-center on-surround antagonistic filters for contrast calculation. The bell-shaped curve between the ANCHORED LIGHTNESS and BHCAW modules illustrates the one-dimensional shape of the blurring kernel for anchoring. For clarity, BOUNDARY SYSTEM shows just one orientation. In the simulation, four orientations are used.

2.1 Retinal Adaptation. The model retina calculates the steady-state of retinal adaptation (light adaptation and spatial contrast adaptation) to a given input image. It adapts the response of photoreceptors to varying levels of incoming light, since otherwise the visual process could be desensitized by saturation right at the photoreceptor. Light adaptation, at the photoreceptor outer segment, protects each photoreceptor from saturation by using intracellular temporal adaptation that shifts the photoreceptor sensitivity curve (GATED INPUT in Figure 9; Baylor, Hodgkin & Lamb, 1974a, 1974b; Carpenter & Grossberg, 1981; Koutalos & Yau, 1996). See Appendix A, equations (A1)-(A3) for this mechanism.

The light-adapted signal is further processed at the photoreceptor inner segment where it gets feedback from a horizontal cell (HC) that is connected with other HCs by gap junctions, forming a syncytium that is sensitive to spatial contrast (Figure 9). HC inhibition further adjusts the sensitivity curve to realize spatial contrast adaptation. It is assumed that the permeability of gap junctions between HCs decreases as the difference of the inputs to HCs from coupled photoreceptors increases. In Figure 9, for example, where the input pattern has a steep difference (the thick and thin input arrows), the permeability between the left and right HCs decreases. When there is not much difference in inputs, the permeability between

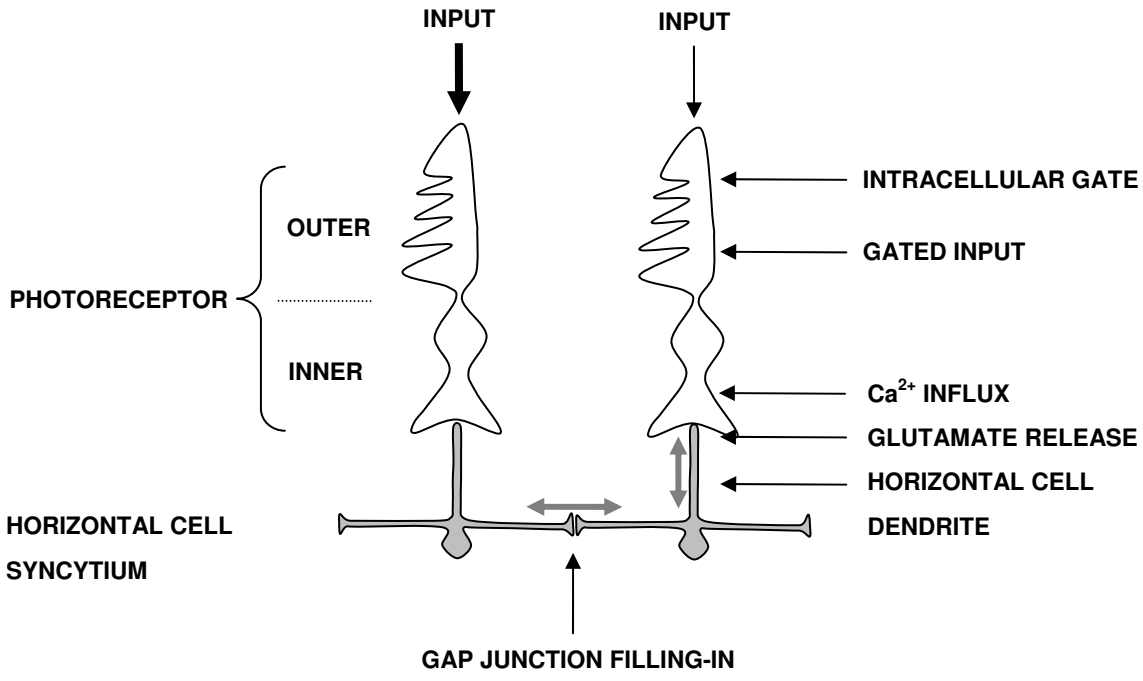

Figure 9. Circuit of retinal adaptation. Two stages of Retinal adaptation are implemented: One light adaptation at the outer segment of the photoreceptors, the other, spatial contrast adaptation at the negative feedback circuit between the inner-segments of photoreceptors and a syncytium of HCs. It is assumed that the permeability of the gap junctions between HCs decreases as the difference of the inputs to the HCs from the coupled photoreceptors increases. For simplicity only the connections between nearest neighbors are shown. In simulations, long-range connections are also allowed. The gray bidirectional arrows show the mutual influence between connected units. See the text and Appendix for further details.

the HCs remains large. The model retina hereby segregates and selectively suppresses signals in regions that have strong contrasts, such as a light source. Figure 9 shows only connections between nearest neighbors. In simulations, connections reaching farther than nearest neighbors are also used that model the connectivity and cell types in the retina (Masland, 2001; Sterling, 1998). Inhibition of the HC on the photoreceptor controls the output of the photoreceptor (GLUTAMATE RELEASE in Figure 9) by modulating Ca^{2+} influx at the photoreceptor inner segment. This feedback prevents the output from being saturated by localized high-contrast input signals. It hereby helps us see a room lit by a light bulb, the light bulb itself, and the label on it. See Appendix A, equations (A4)-(A8).

2.2 Multiple-Scale Contrast and Luminance Stage. The retinally-adapted signal is processed by the Contrast stage, which is realized by center-surround networks. The Contrast stage thus receives normalized input signals. The Contrast stage carries out spatial frequency-specific processing in multiple scales using cell types with ((on-center off-surround)) (ON cells) or off-center on-surround (OFF cells) found in the retina (Barlow, 1953; Cook & McReynolds, 1998; Kuffler, 1953; Werblin & Dowling, 1969) and the lateral geniculate nucleus (LGN) (Dubin & Cleland 1977; Hubel & Wiesel, 1961; Jones et. al., 2000; Schiller 1992). Retinal and LGN mechanisms are lumped together to provide the simplest realization of mechanisms that are needed to derive the desired results. See Appendix A, equations (A9)-(A22).

The 1-D cross-sections of the contrast operators are illustrated in Figure 8 between the RETINAL ADAPTATION and CONTRAST stages. For example, a feedforward shunting on-center off-surround network (Grossberg, 1980, 1983) extracts local contrasts and significantly attenuates illumination gradients and background levels in a scale-specific manner. It does so using automatic gain control that divides the input of the center by the local average represented by the surround, thus estimating the local contrast:

$$\text{Contrast} = \frac{L_{spot} - L_{background}}{L_{spot} + L_{background}},$$

where L_{spot}, and $L_{background}$ are the luminances of the probe stimulus and background, respectively. Using different sizes of surround, the system extracts small-scale to large-scale contrasts. These various surround sizes simulate the different sizes of lateral inhibition cell types in the retina (for a review, see Masland, 2001). The model uses a fixed narrow center kernel with the different surround scales (Grossberg et al, 1995; Mingolla et al, 1999) and thereby also simulates the output of a sharp center at the ganglion cells due to interactions in the retinal network (Cook & McReynolds, 1998; Roska et al., 2000). This is sufficient to simulate the targeted lightness data. Although the shunting center-surround network is presented separately from the retinal adaptation stage, it also contributes to background adaptation. Likewise, the adaptation by the HC network is a type of center-surround process with a large surround scale.

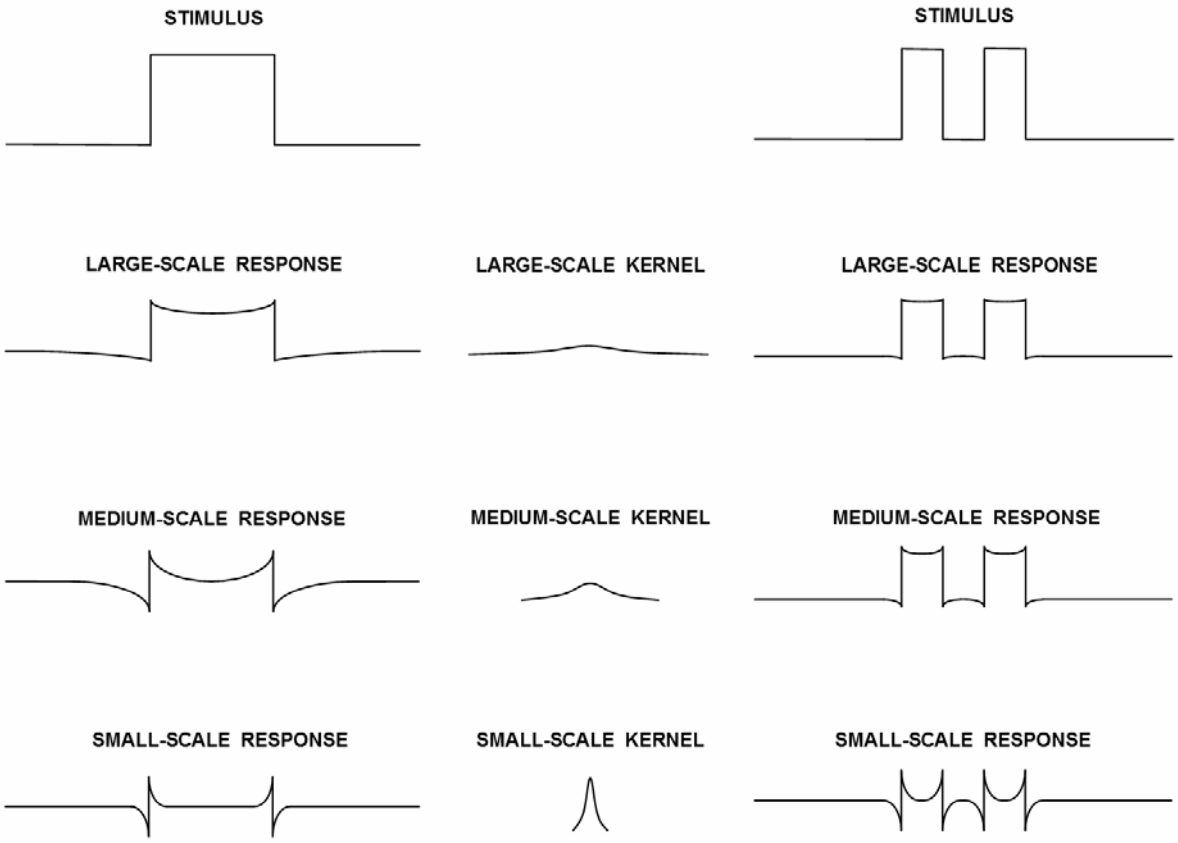

Figure 10. One-dimensional illustration of center-surround processes in different spatial scales. The figure shows two stimuli and corresponding processed signals in different spatial scales in the left, right columns. The surround kernels of different spatial-scales are shown in the middle column. For clarity, the narrow center kernels, whose sizes are the same, are not shown. As a given surface divides into smaller patches, such as from the stimulus on the left to the stimulus on the right, medium and large-scale center-surround processes do not fully activate and fully suppress the homogeneous area. Since the model uses the weighted sum of multiple scale signals, this leads to a more veridical or non-compressed representation. The model takes this contrast calculation mechanism as part of the Articulation, Configuration, and Insulation effects of lightness anchoring. See Lightness Anchoring section for further details.

Figure 10 illustrates how three different scales, that are defined by different Gaussian off-surround filter widths, respond to luminance inputs. Since the large-scale signal represents the luminance signal better (see LARGE-SCALE RESPONSE in Figure 10), it plays the role of a *luminance signal*. In order to preserve image resolution, single-scale models typically use such a small scale. However, a small scale may exhibit *brightness bowing* (see SMALL-SCALE RESPONSE in Figure 10) because a small-scale (high frequency) center-surround unit acts like an edge detector, and thereby suppresses information from large homogeneous surface regions.

The model postulate of multiple scales is consistent with electrophysiological observations in V1 of alert primates (Bartlett & Doty, 1974; Kayama et al., 1979; Kinoshita & Komatsu, 2001; Komatsu, Murakami & Kinoshita, 1996) and anesthetized cats (MacEvoy, Kim & Paradiso, 1998), where cells code not only edge signals but also uniform surface luminance as well. The electrophysiological study with alert monkeys by Friedman et al. (2003) also shows that cells in V1 and V2 code uniform color surface information. In the LGN, uniform surface luminance coding units have been found in anesthetized primates (Marrocco, 1972) and cats (Papaioannou & White, 1972) as well as in alert primates (Barlow, Snodderly & Swadlow, 1978; Kayama et al., 1979). When surface luminance was temporally modulated, cells in the LGN and V1 of anesthetized cats coding the surface region were modulated (Rossi et al, 1996; Rossi & Paradiso, 1999). Kahrilas, Doty, and Bartlett (1980) failed to detect such neurons in visual cortex of the awake rabbit. Their data suggest that there may be some differences between species, and techniques of anesthesia also seem to play an important role.

2.3 Boundary Formation. Boundary-gated filling-in has helped to simulate many psychophysical and neural data about surface perception (Arrington, 1994; Cohen & Grossberg, 1984; Grossberg & Mingolla, 1985a, 1985b; Grossberg & Kelly, 1999; Grossberg, Hwang & Mingolla, 2002; Kelly & Grossberg, 2000; Pessoa, Mingolla & Neumann, 1995). Grossberg & Todorovic (1988) developed this concept to simulate psychophysical data about brightness (perceived luminance). In their model, the illuminant is discounted by a contrast-detecting on-center off-surround network among cells obeying shunting equations. The surviving contrast signals are used to fill-in a surface brightness estimate within a region surrounded by boundaries that are themselves derived from the illuminant-discounted contrast signals. The Anchored Filling-In Lightness Model (aFILM) adopts this hypothesis to explain lightness data using contrast and luminance signals together to trigger filling-in of lightness in regions that are defined by surrounding boundaries (Figure 8). The filling-in mechanism is, however, assumed not to be diffusion, but rather a much more rapid propagation of signals using long-range horizontal connections.

Simple cells. Boundary formation begins at model simple cells that simulate orientationally-tuned simple cells in layer 4 of cortical area V1 (Figure 8), which have contrast-polarized and oriented ON (excitatory for luminance) and OFF (excitatory for darkness) regions in their receptive fields (Bullier & Henry 1979; Gilbert 1977; Hubel & Wiesel 1962). Model simple cells pool model ON cell LGN outputs in their ON region and OFF cell LGN outputs in their OFF region, consistent with data showing that the ON and OFF subfields of simple cells originate from projections of ON and OFF cells in the LGN, respectively (Alonso, Usrey & Reid 2001; Lee et al., 2000; Reid & Alonso, 1995). Receptive fields of a simple cell are modeled by a pair of elongated Gaussian kernels with shifted centers (Grossberg, Mingolla & Williamson, 1995; Mingolla, Ross & Grossberg, 1999; Pessoa, Mingolla & Neumann, 1995). The model simple cell is maximally active when a luminance edge is aligned with the oriented border between the ON and OFF regions due to a push-pull design of the ON and OFF regions. For example, a simple cell with a vertical orientation and a light-dark polarity from left to right pools excitatory inputs from on-

center off-surround contrast signals on the left side of the kernel and off-center on-surround signals from the right side of the kernel, and also pools inhibitory inputs from on-center off-surround contrast signals on the right side of the kernel and off-center on-surround signals from the left side of the kernel. Since the output is a rectified sum of the filtered signals, the simple cell is active only when a luminance imbalance occurs with the correct polarity across the oriented axis. See Appendix A, equations (A25)-(A32).

Complex cells. The boundary signals of an object need to be joined together even in cases where a scene's contrast polarity reverses along the border of the object, such as at the edge of a middle gray object on a white-and-black checkerboard background (Grossberg, 1994). The model does this using model complex cells that pool a pair of light-dark and dark-light simple cell signals of the same orientation at each position. Pooling simulates the known complex cell property of responding to oriented luminance edges without clear ON/OFF subfield zones (Mechler & Ringach, 2002). See Appendix A, equation (A33). A hierarchical combination of simple cell outputs at complex cells (Hubel and Wiesel 1962; Schiller, Finlay & Volman, 1976) is supported by recent experimental data (Alonso & Martinez, 1998; Dresp & Grossberg, 1997; Martinez & Alonso, 2001), theoretical analysis (Sakai & Tanaka, 2000) and modeling studies (e.g., Gove, Grossberg & Mingolla, 1995; Grossberg & Mingolla, 1985a). Additional feedback interactions exist (see Raizada and Grossberg, 2003), but are not needed for present purposes.

2.4 Surface Filling-In. At the Surface Filling-In stage, cells pool signals from both the Contrast and the Luminance stages. Three scales are pooled: Small-scale and medium-scale contrast signals and large-scale luminance signals. See Appendix A, equation (A38). These pooled signals fill-in along long-range horizontal connections, a new model feature. See Appendix A, equations (A40)-(A44). Filling-in is blocked by signals from the Boundary System stage.

As noted above, boundary-gated surface filling-in has been used to explain many psychophysical data about brightness and color perception and 3D figure-ground perception. The filling-in mechanism utilizes two streams of the What cortical visual pathway: The surface stream has been predicted to run through the blobs and V2 thin strips to V4, whereas the boundary stream runs through V1 interblobs and V2 pale stripes to V4 (Grossberg, 1994). These two streams have been proposed to compute complementary properties during visual information processing (Grossberg, 2000). A growing list of experiments support the existence of such a filling-in process. The important psychophysical study of filling-in by Paradiso and Nakayama (1991) attempted to catch filling-in "on the fly." Arrington (1994) used the Grossberg and Todorovic (1988) model to fit the Paradiso and Nakayama (1991) data about the dynamics of filling-in. The dynamics of aFILM are consistent with the Arrington (1994) explanation.

Filling-in in the blind spot is another example of surface filling-in (Komatsu et al., 1996, 2000). Surface representations can be formed early in visual processing even without top-down cognition signals (Kamitani & Shimojo, in press). Sasaki et al. (2001) showed using fMRI that when a human subject perceives a transparent illusory region bounded by illusory contours, the V1 region corresponding to the

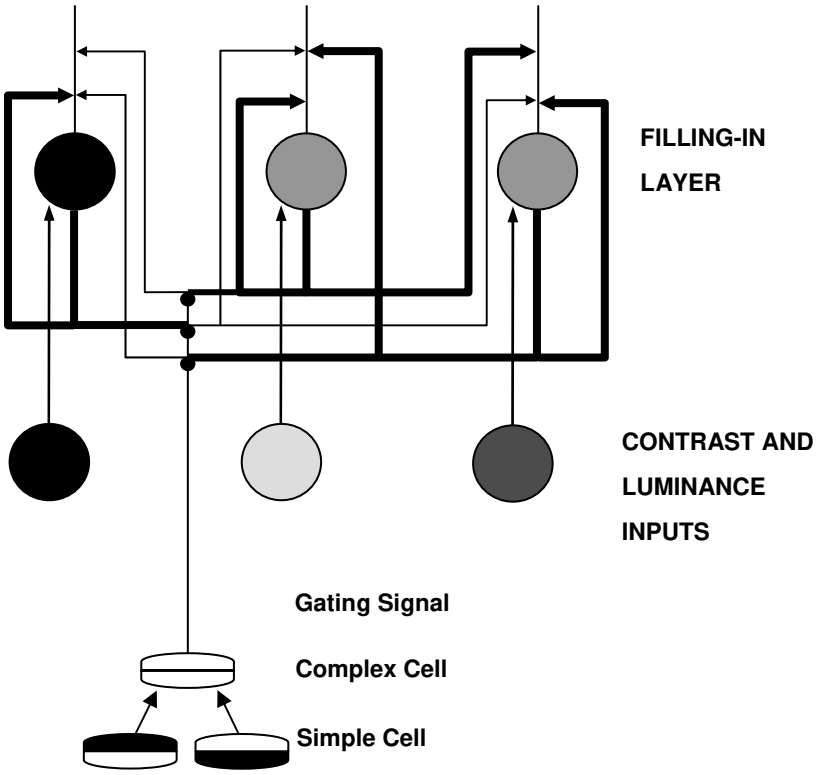

Figure 11. Schematic representation of the parallel filling-in mechanism. In the filling layer, the signals coming from the contrast and luminance units are homogenized within areas defined by luminance boundary signals. The horizontal connections that propagate signals are gated by the gating signals coming from the complex cells. The gated lateral connections have smaller conductances (thin lines) than the other ones (thick ones). The gray levels in the round units represent the activities of them. Just one set of gating signal is shown for clarity.

illusory visual field became active. These data, combined with data about illusory contour representations known to exist in V2 (von der Heydt, Peterhans, & Baumgartner, 1984), are consistent with the possibility that surface representations may start to form in V2. More direct evidence comes from electrophysiology combined with cortical imaging: Hung et al. (2001) reported that the Craik-O'Brien-Cornsweet Effect can be detected in V1 and is prevalent in V2. In their experiment, the activities of cells having receptive fields inside the homogeneous surfaces were modulated with cusps at the edge of the surfaces. The large spatial scale needed to fully integrate information across visual space (Angelucci et al., 2002) also marks V2 as a processing stage where surface representations start to get formed. Data concerning border ownership representations in V2 and V4 (Zhou et al., 2000) are also consistent with this conclusion. See Grossberg (1994, 1997) for further discussion.

Figure 11 shows a 1-D illustration of the model filling-in network. The round units on top represent the cells in the Surface Filling-In stage. The cells in the Contrast and Luminance stage feed their signals topographically to the corresponding filling-in cells. These signals spread between filling-in cells along long-range horizontal connections with Gaussian receptive fields. Signal propagation is gated by Boundary System signals (represented by a vertical line in Figure 11) coming from the complex cells (for simplicity just one set of gating cells is shown). The gated horizontal connections have smaller conductances (thin horizontal lines) than the other ones (thick horizontal lines). The gray levels of the filling-in cells and of the contrast and luminance input cells represent the level of cell activation. The FILLING-IN LAYER illustrates two homogeneous filled-in regions, black and middle gray, separated by a boundary signal.

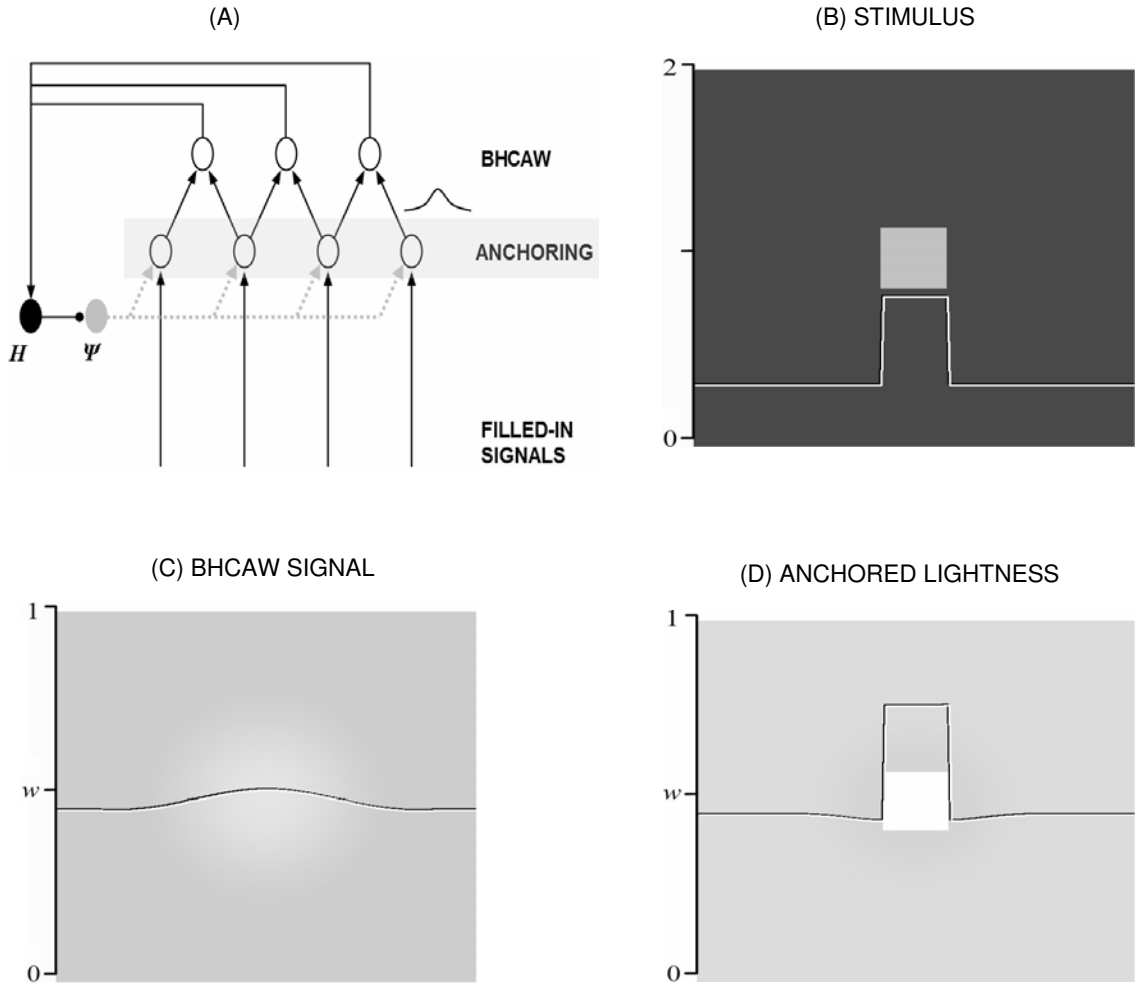

Figure 12. BHCAW rule and Area Effect in a two-field Ganzfeld configuration. (A) Model circuit of lightness anchoring. The activities of the ANCHORING units are locally pooled by BHCAW units to form a blurred version of the ANCHORING signals. The filter used to generate the blurred signals is shown as a bell-shaped figure between the ANCHORING and BHCAW modules. The BHCAW signals are fed to an inhibitory unit *H*. The unit *H* becomes active when any of the BHCAW unit exceeds its threshold set to WHITE and fires. When active, *H* inhibits the tonically active unit *Ψ* that modulates the activities of ANCHORING units. This circuit allows the activities of ANCHORING units to grow until at least one of the blurred version of anchoring signals, BHCAW, meets the criterion of WHITE. See Appendix A for mathematical details. One thing to notice is that the inhibition by *H* on *Ψ* lowers but does not completely shut off the activity of *Ψ*, leaving a chance to the BHCAW signals to go beyond WHITE when the bottom up signal is strong enough, for example, a bright light source of some size. In such a case, even the BHCAW rule will be violated. (B-D), Two-dimensional simulation of two-field Ganzfeld configuration. The curve on each figure represents the activities of the units along the horizontal midline. This convention applies to all the following figures. The scale for the curve is denoted on the left side of each figure. B.STIMULUS shows the input configuration. D.ANCHORED LIGHTNESS shows the area effect corresponding to the one in Figure 4B. Note that the highest activity of the BHCAW module in Figure C is anchored to white (*w*).

2.5 Anchored Lightness. Anchored Lightness stage cells receive inputs from the Surface Filling-In stage. These cells are modulated by a feedback signal originating from the anchoring cells themselves that renormalizes their activities to realize an absolute lightness scale (Figures 8 and 12A). As noted in Section 1.3, the new Blurred-Highest-Contrast-As-White (BHCAW) anchoring rule overcomes problems of the classical HLAW rule. See Appendix A, equations (A45)-(A53), for the anchoring equations.

Figures 3A and 3B illustrate the model's explanation of the area effect for a two-field Ganzfeld configuration, as in Figure 7. In such a display, there are just two homogeneous surfaces with different luminances, one the target surface, the other the Ganzfeld. To achieve anchoring, the model first computes a blurred version of the filled-in surface activity, called the BHCAW signal (Figure 12A). The highest value of this blurred pattern is anchored to white by using a feedback signal, labeled ψ (Figures 8 and 12A), that multiplicatively rescales the filled-in surface signals by automatic gain control. The process H, which inhibits ψ, becomes activated whenever any BHCAW signal exceeds a threshold that determines the value of white (WHITE in Figures 3A and 3B). Since the highest value of the *blurred* filled-in activity is used for anchoring, the anchored lightness (ANCHORED LIGHTNESS), or unblurred pattern, will look self-luminous (Figure 3B) when the area of the highest filled-in activity is not broad enough to span the blurring kernel. This happens because the blurring kernel averages lower activities as well at this position, so WHITE will be a smaller value than the maximum filled-in activity. As the area of the highest filled-in activity becomes larger, this mechanism predicts that the background will approach WHITE because of the small difference between the highest and background signals that are averaged by the blurring kernel (Figure 3A). Figures 12B to 12D show a 2-D simulation of the two-field Ganzfeld configuration. The curve in each figure shows the activities of the cells along the horizontal middle section of the 2-D image. The labels on the left side of each figure indicate the scale of vertical axis for the curve; in particular, w denotes white.

3. Simulation Results

The first results demonstrate that the model can simulate various classical lightness properties, while also anchoring the results.

3.1 Light Adaptation. As noted in Section 1.1, the model retina can realize light adaptation properties; see Figures 1A and 1B. Figure 1C illustrates the shift of retinal sensitivity with background illumination that makes model light adaptation possible. This shift property emulates neurophysiological data of Werblin (1971), among others. The leftmost curve of the shift property at lower values of background luminance corresponds to the physical limit of light adaptation observed in retinal ganglion cells (Barlow & Levick, 1969; Enroth-Cugell & Shapley, 1973a). Over a wide range of background luminances, the model obeys the classical Weber law (Grossberg, 1983). Intracellular temporal adaptation in each photoreceptor acts like a divisive negative feedback signal. See Appendix B for stimuli used in this simulation.

3.2 Lightness Constancy and Discounting Illumination Gradients. Figures 13A and 13B illustrate how the model discounts the illuminant in response to two light patches on a dark gradient of illumination in the background. To generate the input, light patches with the same reflectance and a background with a smaller constant reflectance were multiplied by a gradient of illumination. The curves on Figures 13A and 13B show the input intensities and anchored lightnesses along the horizontal midline, respectively. Figure 13B shows the property of lightness constancy and illumination discounting: The light patch on the left is almost as light as the one on the right, unlike the one in Figure 13A. This property comes from the ratio-calculating property of the local contrast units. Figure 13B also shows that, when the gradient of illumination is big enough, the model exhibits a lightness bias where the square patch with higher illumination looks slightly lighter than the one with lower illumination This property is due to the large scale that computes a more veridical representation of the stimuli. This prediction is supported by the observation that, when subjects are asked to decide the perceived reflectance of surfaces, they always give a higher value to the highly illuminated one than the same one with low illumination. (Gilchrist et. al., 1999, p. 826).

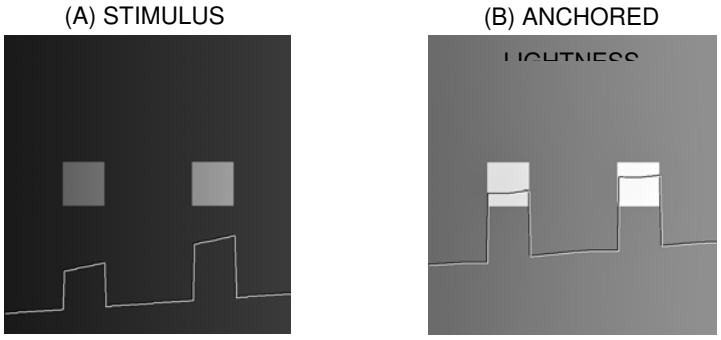

Figure 13. Discounting illuminant. Unevenly illuminated two light patches with identical reflectance (A.STIMULUS) generate a percept that discounts the illumination (B.ANCHORED LIGHTNESS). However, the model also predicts a bit of bias introduced by the illumination gradient. The light patch on the right looks a bit lighter than the left one. The model also picks up the illumination gradient itself using the large scale.

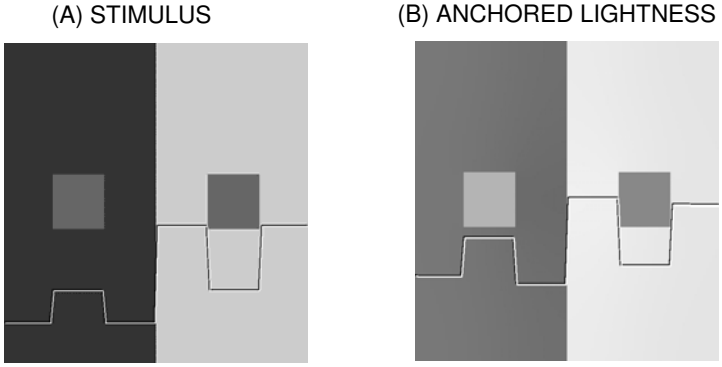

Figure 14. Simultaneous contrast. Two identical square patches on different backgrounds (A.STIMULUS) are perceived differently (B.ANCHORED LIGHTNESS). The one on the dark background looks lighter. Local contrast signals provide the source of this difference.

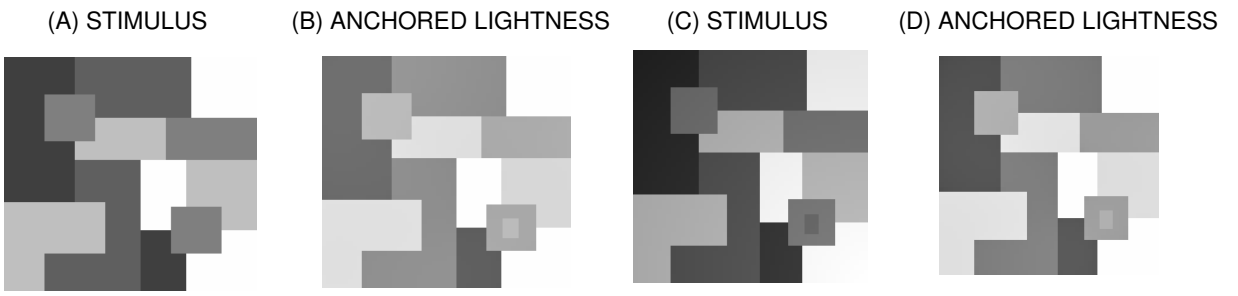

Figure 15. Evenly and unevenly illuminated Mondrians. To facilitate the comparison, a part of the square on the upper left of each figure has been cut and pasted to the square on the bottom right of the figure. (A-B) Evenly illuminated Mondrian. STIMULUS and ANCHORED LIGHTNESS panels show the configuration of an evenly illuminated Mondrian stimulus and the output of the model, respectively. (C-D) Unevenly illuminated Mondrian. The STIMULUS shows the differently illuminated target surfaces because of the illumination gradient. The gradient of illumination is made by a light source located at the bottom-right corner. ANCHORED LIGHTNESS shows the final output of the model. See the text for details.

3.3 Lightness Contrast. Figure 14 shows a simulation of lightness contrast. The two middle gray patches in Figure 14A have identical luminance. Small and medium scales calculate local ratio contrasts, and their contribution makes the light square on the dark background look lighter than the one on the bright background, even though they have identical luminance (Figure 14B).

3.4 Contrast Constancy: Evenly and Unevenly Illuminated Mondrians. Figures 15A and 15B show an evenly illuminated Mondrian and the corresponding model percept, respectively. A part of the square on the upper left of each figure is cut and pasted into the square on the bottom right. Since both squares have the same luminance, Figure 15A shows no cut patch in the bottom right square. Figure 15B shows that the square on the top left is perceived to be lighter than the bottom right square, because the square on the right bottom is surrounded by lighter surfaces than the square on the left top. The square on the right bottom thus receives more surround suppression than the square on the upper left.

Figures 15C and 15D show that the model generates the same result when a light source at the bottom right corner creates a gradient of illumination from bottom right to top left. The model output (Figure 15D) shows that the upper left square still looks lighter than the bottom right square despite the fact that the luminance at the bottom right is higher. This happens because the small and medium scales calculate the local contrasts and ignore the large scale illumination gradient. This "contrast constancy" calculation by the two smaller scales overrides the prediction by the big scale that picks up the gradient. Grossberg and Todorovic (1988) first simulated this effect with a single contrast scale.

3.5 Craik-O'Brien-Cornsweet Effect. The Craik-O'Brien-Cornsweet effect (Cornsweet, 1970) is challenging because filtering alone cannot explain the percept. As with the percepts above, the model explains this illusion using a combination of illuminant-discounting filtering followed by boundary-gated

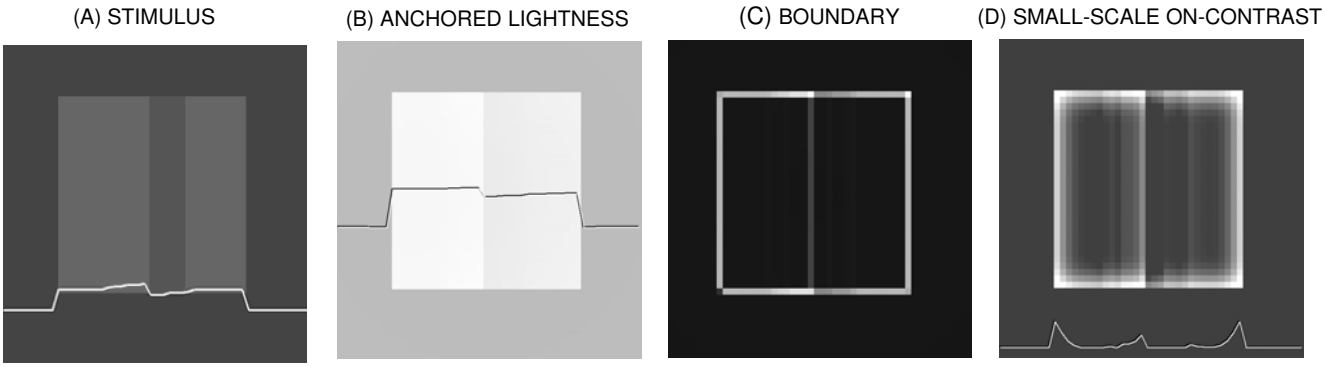

Figure 16. Craik-O'Brien-Cornsweet effect. (A) Two divided identical surfaces with a luminance cusp in the middle. (B) Simulated lightness of the model. The two surfaces are perceived differently. The boundary-gated homogenization of surface signals through a filling-in process makes the surface on the left look slightly lighter than the one on the right. (C) Boundary. (D) Small-scale contrast signals for the two surfaces. Left surface has more activities than the right one explaining the difference at the filled-in surface lightnesses in B.

surface filling-in, as first simulated in Grossberg and Todorovic (1988). Figure 16A shows the stimulus with a uniform background luminance with a luminance cusp in the middle. Figure 16B shows the anchored lightness percept in which the left half of the image looks uniformly lighter than the right half. At the Surface Filling-In stage (Figure 8), the cusp-like inputs from the Contrast stage (Figure 16D) are smoothed within areas defined by Boundary stage signals (Figure 16C). This smoothing makes the surface on the left lighter than the one on the right because of the larger contrast activities within this region (Figure 16D). The area-defining boundaries play a critical role. When no boundaries surround the luminance cusp, the illusion is not seen because the contrasts can spread via filling-in around both sides of the cusp region and smooth one another; see Grossberg and Todorovic (1988).

3.6 Double Brilliant Illusion. Bressan (2001) described a Double-Brilliant illusion wherein the diamond that has less contrast around it (Figure 17B) looks more brilliant than the one having more contrast around it (Figure 17A) even though both diamonds have the same luminance (Figure 17C). How this brilliant appearance gives rise to a judgment of "lightness" may depend on subtle stimulus matching properties in a particular experiment. Bressan (2001, p. 1042, caption of Figure 8) writes: "Both diamonds are white, and mounted on luminance-ramp settings. But the diamond sitting on the dark end of the ramp (left) looks whiter than the one sitting on the light end of the ramp (right)." There do not seem to be any parametric psychophysical data, however, to characterize the nature of the judgment, which may include a variety of factors, including cognitive ones.

The model simulates the more brilliant appearance of Figure 17B as a manifestation of spatial contrast adaptation, as in Figure 1D and 1E (see Appendix A, equations (A4)-(A8)), and thereby raises the issue of what additional perceptual processes or criteria might lead to the claim that Figure 17A is lighter. In particular, the permeability of gap junctions in the horizontal cell (HC) syncytium decreases

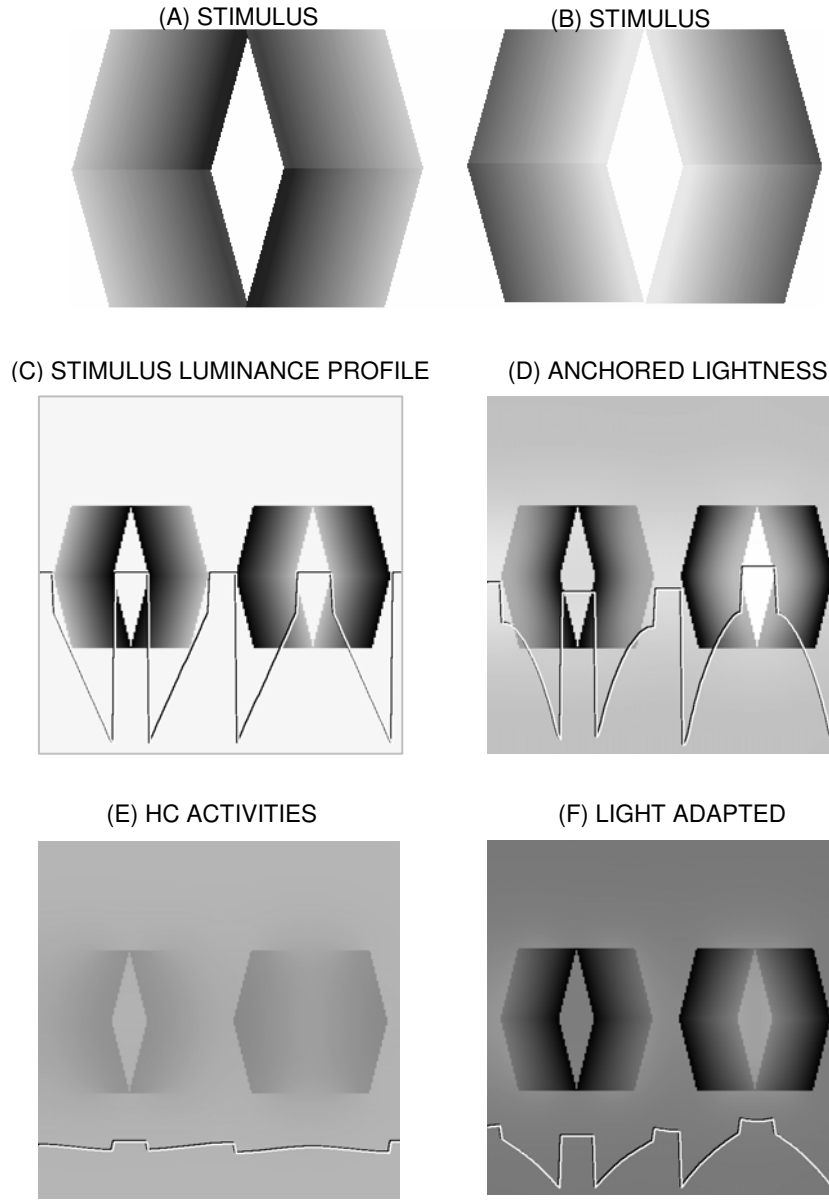

Figure 17. Double Brilliant Illusion. (A-B) Stimuli. A psychophysical experiment shows that the diamond part of the stimulus B looks lighter than that of the stimulus A. (C-D) Stimulus and the output of simulation, respectively. (E-F) Simulated activities of HCs and the steady outputs of photoreceptor inner segments, respectively. See the text for more details. The figures A and B are from Bressan (2001).

only where there is a sharp luminance edge in the input (Figure 9). The gradual change of luminance around the diamond in Figure 17B does not block the diffusion of signals across the HC syncytium. The luminance edges around the diamond in Figure 17A do block diffusion and segregate the diamond region from the rest of the figure. This gated-diffusion process is simulated in Figure 17E. The segregated large signals shown in the diamond region on the left of 17E suppress the corresponding region of photoreceptor outputs. This results in a less active diamond region on the left in Figure 18F compared to the diamond region on the right. The anchored lightness of the model in Figure 18D reflects this difference. The model interprets the contrast adaptation mechanism to be retinal, hence monocular. If this

is a correct assumption, then dichoptic presentations of different stimulus parts to each eye may yield different lightness effects. Figure 1D-E and Section 4.1 around Figure 18 show how spatial contrast adaptation can greatly facilitate perception of scenes with large contrast differences.

3.7 Anchoring Properties. In addition to simulating classical lightness effects, the model also simulates, for the first time, the four major effects of lightness anchoring (Articulation, Configuration, Insulation, Area Effect) that have been described by Gilchrist and his colleagues:

***Articulation effect*:** The Articulation effect says that, as the display contains more gray surfaces, the range of perceived lightness widens (Figures 4A-4F). Even in the two-Mondrian case in Figure 4C, the reflectances of these patches range from black to white, covering the full span of reflectance. Adding more gray patches does not result in a wider range of reflectances. Figure 4G summarizes the model simulation. As the number of surface patches having different luminances increases, the image contains more high spatial frequencies. The medium and large spatial scale kernels thus have less chance to fully activate and suppress the homogeneous area of each patch. Figure 10 illustrates the situation: The divided square luminances on the right cause higher contrast signals in the medium and large scales compared to the corresponding contrast signals on the left column with a larger square stimulus. The loss of suppression by each spatial scale results from the mismatch between the size of the filters and of the scenic patches. Mismatch means less suppression, thus a more veridical representation for that scale, and thus a more veridical percept. The BHCAW process assures that the data remain anchored at white.

***Configuration effect*:** The Configuration effect says that, when a display contains gray surfaces arranged in a Mondrian, a wider range of lightnesses is perceived than when the same gray surfaces are arranged in a luminance staircase. Figures 5E and 5F summarize model simulations. The model explains this effect much as it does the Articulation effect: In the Mondrian, the intermingled luminance patches are arranged in a more radially compact way. The round-shaped surround kernels in the Contrast stage are thus influenced by more luminances of surrounding surfaces compared with the staircase arrangement. This lets the surround kernels set the local means (surround activities) to be more different from the corresponding center activities, resulting in a bigger range of perceived reflectances. In other words, if all the adaptation and contrast stage surround activities were the same as their center activities, surround inhibition would drive them all to zero. The radially compact arrangement decreases the distance between different levels of gray patches, thereby inducing stronger lateral inhibition. The influence of the distance between an inducer and test surfaces has been observed in lightness (Newson, 1958) and brightness experiments (Cole & Diamond, 1971; Fry & Alpern, 1953; Leibowitz et al., 1953), where the darker test surface became lighter with increasing distance from the inducer due to surround inhibition. Again, BHCAW process anchors the perception of white.

***Insulation effect*:** The Insulation effect of Figure 6 shows that, when the staircase display is insulated by a white surround, the range of its perceived reflectance widens. Figures 6D and 6E show the data and simulation results, respectively. Spatial contrast also helps to explain this effect: Insulation of

gray surfaces with a white surround results in an expansion of the range of lightness due to the newly added suppression on dark patches by the surround. Insulation by a black surround, however, may not cause much difference because the gray surfaces are illuminated 30 times more than the background. Since the gray patches are already not getting much background inhibition, introducing black insulation does not significantly change the amount of inhibition, thus hardly changing the percept. The BHCAW process again anchors the lightness.

***Area effect*:** The Area effect in Figure 7 shows that, in a two-field Ganzfeld situation, as an area other than the area of highest luminance becomes larger than the half of the visual field, its lightness approaches white while the highest luminance area is pushed above white. Figure 8C shows the model simulation, which closely fits the data. Section 2.5 predicts how self-luminosity of a small highest luminance area may be explained by the BHCAW rule: When the highest luminance area is smaller than the blurring kernel at the anchoring stage, the blurred filled-in surface signals will have lower highest activities compared to the un-blurred image (Figures 3B). Since blurred signals anchor lightness, the highest luminance area will look lighter than white. Figure 3B corresponds to the increasing portions of curves in Figures 8B and 8C, whereas Figure 3A corresponds to the flat regions of these curves.

4. Discussion

The BHCAW model integrates known neuroanatomy, electrophysiology, and psychophysics (e.g., Table 1) to clarify how the brain generates a representation of surface lightness. The following discussion analyzes the model's assumptions and limitations.

4.1 Retinal Adaptation. The model simulates retinal adaptation using two mechanisms; see Figure 9. First, at the outer-segment of the photoreceptors, the model realizes an intracellular mechanism of light adaptation whose sensitivity to light is controlled by concentrations of chemicals, such as Ca^{2+} ions, that temporally average visual stimuli (Koutalos & Yau 1996). Carpenter and Grossberg (1981) used such a mechanism to quantitatively simulate the Baylor, Hodgkin, & Lamb (1974a, 1974b) data about turtle cone adaptation. Second, at the inner-segment of the photoreceptors, the model simulates spatial contrast adaptation by modulating gap junction communication between horizontal cells (HCs) and thus how HCs influence glutamate release from the photoreceptor (Fahrenfort et al., 1999; Verweij et al., 1996) The permeability of HC gap junctions is affected by various mechanisms, including neurotransmitters (DeVries & Schwartz, 1989, 1992; McMahon, 1994; Xin & Bloomfield, 2000) and transjunctional voltage (Lu et al., 1999; Spray et al., 1979).

For example, for two HCs connected by a gap junction, the permeability of the junction decreases as the difference increases between the inputs that the HCs receive from the photoreceptors (Figure 9). Such a model retina can properly rescale inputs that have too much contrast, such as the one in Figure 18A. Figure 18D shows the steady-state HC activities; the dark and light image regions deliver different

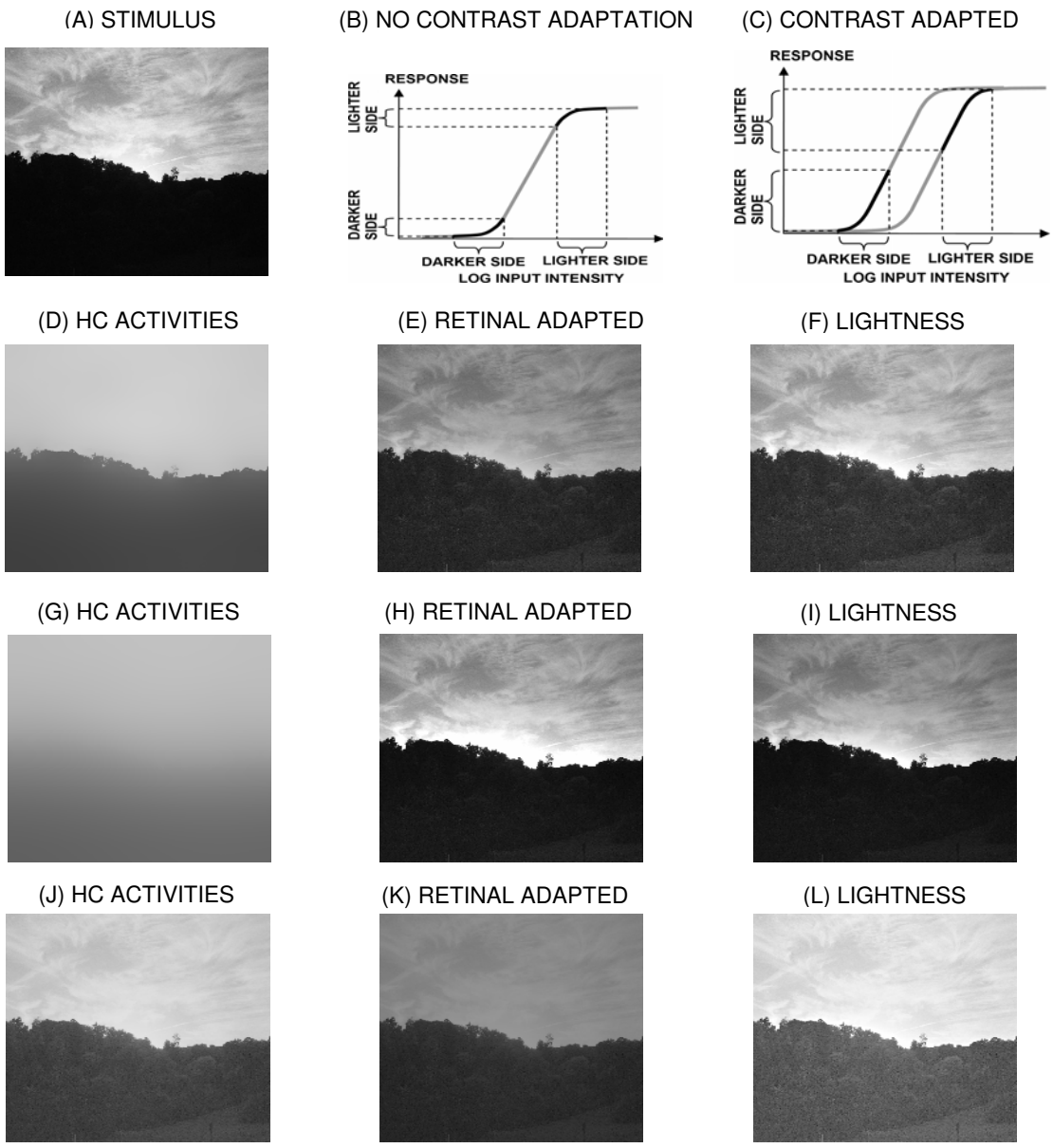

Figure 18. Effect of gated diffusion for spatial contrast adaptation of the model. (A) Stimulus. (B) Illustration of retinal sensitivity curve with no contrast adaptation. The signals for the dark part (DARKER SIDE along the abscissa) have been mapped to the very low part of the response axis (DARKER SIDE along the ordinate). The signals for the light part (LIGHTER SIDE along the abscissa) have been mapped to the saturating portion of the curve (LIGHTER SIDE along the ordinate). (C) Illustration of contrast adaptation. With the two different sensitivity curves, the model retina has mapped the widely separated input signals (DARKER SIDE and LIGHTER SIDE along the abscissa) to quite "visible" portions of the response (DARKER SIDE and LIGHTER SIDE along the ordinate). (D) The steady-state activities of HCs at the input A. (E) Retinally adapted signals. Retinal adaptation with gated diffusion at the HC syncytium gives the properly rescaled steady-state output at the inner-segment of the photoreceptor. (F) The final output of the model. (G-I) Simulation with free diffusion among connected HCs. (J-L) Simulation with no diffusion among HCs. See the text for further details

suppressive feedback signals to the photoreceptors. Figure 18B shows how the retina would respond without spatial contrast adaptation; note that the responses at both the darker and lighter sides of the image are highly compressed, hence insensitive to input contrast differences. Figure 18C shows how spatial contrast adaptation generates two distinct sensitivity curves at photoreceptor inner-segments due to the two different negative feedback levels of the HC network. The network hereby rescales responses at the inner-segment of the photoreceptor to be more sensitive to input contrast differences at both darker and lighter image regions. The rescaled steady-state output of the photoreceptor inner-segments are shown in Figure 18E. The output of the model photoreceptor in Figure 18F shows visible dark and light image regions. Figures 18G-I show a simulation without the HC gating mechanism. The adapted signals in Figure 18H and the output in Figure 18I show signal distortion (a halo) along the border of the dark and light parts, and the dark part is less visible. Figures 18J-L show a simulation with no diffusion among HCs. The results show a prominent compression of signals.

In summary, in addition to the light adaptation at the outer-segment of the photoreceptor, which shifts its sensitivity curve, HC negative feedback further shifts photoreceptor sensitivity in response to the spatial context of input contrasts. See Appendix A, equations (A1)-(A8).

Kamermans et al. (1996) discussed how negative feedback between the photoreceptor and the HC network might influence the length constant of the HCs. The present analysis does not need this refinement to quantitatively explain the targeted data. For the same reason, the model also does not simulate the cone-rod circuitry switch (Mills & Massey, 1995; Ribelayga, Wang & Mangel, 2002) and the pupillary light reflex (Dowling, 1987), which also influence adaptation.

4.2 Luminance and Contrast: Multiple-Scale Filtering. The neuroanatomy of the retina already includes multiple-scale representations whereby center-surround processes shape the outputs of ganglion cells having diverse receptive field sizes (Masland, 2001; Roska et al., 2000; Werblin, 2001). The V1 map includes cells whose optimal spatial frequencies increase as their positions move away from blob centers (De Valois & De Valois, 1988; Edwards et al., 1995). Issa et al. (2000) also show gradual changes in cell spatial frequency preferences that conform to the hypercolumn cortical organization in V1. Data about cell responses in LGN, V1 and V2 to uniform surface luminance and color also support the existence of large spatial scales (Bartlett & Doty, 1974; Friedman et al., 2003; Komatsu, 2001; Marrocco, 1972; Papaioannou & White, 1972). The model hypothesis that achromatic cells in the blob stream pool their multiple-scale representations has not yet been directly tested. The pooling of ON and OFF signals, however, is consistent with the finding that the segregation of ON and OFF channels from the retina and LGN, and their projection to layer 4 in V1 is largely lost in the cortex of the ferret (Chapman & Gödecke, 2002). See Schiller (1992) for a review.

Multiple-scale filtering mechanism has also been proposed as part of a recent evolution of Retinex (Jobson et al., 1997a, 1997b; Rahman et al., 1996, 1997). Instead of using predetermined multiple-scale filters all the time and everywhere on the image, the current model reconfigures the shape

of the filters to meet the demanding contexts for a given image using the horizontal gating system (see Appendix A. Retinal adaptation). For example, when there is a bright spotlight like the one in Figure 2G, the HC filters around the edge of the spot light would shrink by disconnecting the communication between the light and the surrounding dark areas using the diffusion gating mechanism illustrated in Figure 2. The result of this dynamic control of the shape of the HC filters is a natural-looking compression of input signals as illustrated in Figure 18 where the two extreme input areas (Figure 18A, Figure 18 DARKER SIDE, LIGHTER SIDE) are pulled in to the visible area (Figure 18C, Figure 18E). The competence of this mechanism has been demonstrated and compared with Retinex in Hong & Grossberg (2004, Section 3.5), where enhanced visibility is demonstrated without sacrificing a natural appearance.

4.3 Boundary Representation. The model's Boundary System stage does not, for simplicity, implement the boundary completion property whereby the visual system forms perceptual groupings from disjoint image inducers (Field, Hayes & Hess, 1993; Grossberg & Mingolla, 1985a, 1985b; Grossberg & Raizada, 2000; Kellman, & Shipley, 1991; Raizada & Grossberg, 2001; von der Heydt, Peterhans & Baumgartner 1984). Incorporation of this property would explain more psychophysical data about such properties as illusory contours (Gove, Grossberg & Mingolla, 1995; Grossberg & Mingolla, 1985a), 3-D figure-ground separation (Grossberg, 1994; Kelly & Grossberg, 2000), and surface noise suppression in response to noisy images (Grossberg et al., 1995; Mingolla et al., 1999). Surface noise suppression in response to noisy images is necessary because visual signals that reach the retina are distorted and occluded by the retinal layers, blind spot, and veins. Boundary completion by bipole cells can group pixels from such noisy images into coherent boundaries that define object contours. Surface filling-in smoothes pixel values that are surrounded by the same boundaries and thus allows the brain to distinguish between noisy signals due to preprocessing artifacts and those that represent object properties. For figures that do not require significant boundary completion, surface noise suppression can be achieved by the present model's simplified boundary and surface filling-in properties, as illustrated by Figure 19D. Figure 19C uses a smaller boundary-gating parameter than Figure 19D, hence smoothes the Lena image less.

4.4 Surface Filling-In. A new mechanism of surface filling-in, called Gated Blurring, uses propagation via long-range horizontal connections that are predicted to be within cortical layer 2/3 of V2, among other places. Previous models used nearest-neighbor diffusion for filling-in. Both types of model predict that filling-in is gated by boundary signals that block signal propagation across positions at which luminance contrasts are registered (Figure 11). This prediction of the model is consistent with the known horizontal connections in the visual cortices (Angelucci et al., 2002; Gilbert & Wiesel, 1979; Rockland & Lund, 1982; Stettler et al., 2002; Yabuta & Callaway, 1998). Long-range horizontal connections have previously been predicted to carry out boundary completion via cells in layer 2/3 of cortical areas V1 and V2 (Grossberg, 1999; Grossberg & Mingolla, 1985a, 1985b; Grossberg and Raizada, 2000; Grossberg &

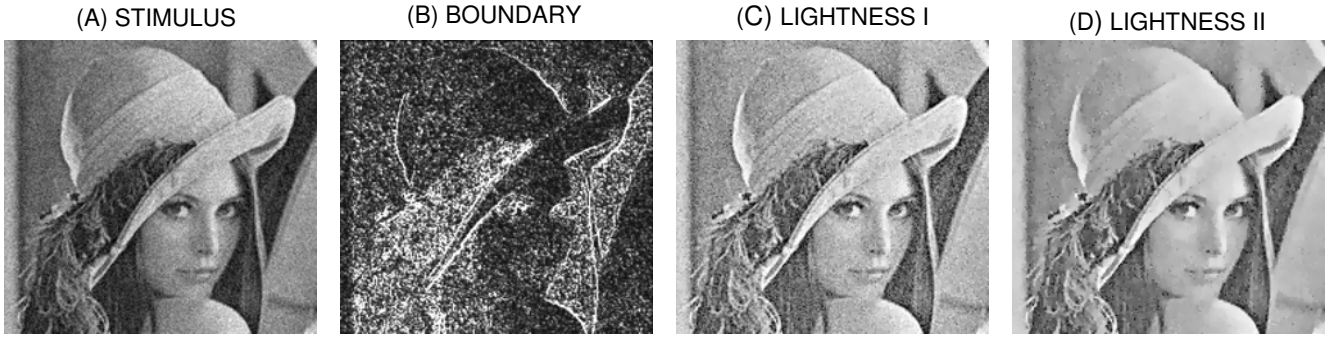

Figure 19. Noise suppression property of the model. (A) Input with Gaussian noise of signal-to-noise ratio of 10 dB. (B) Boundary signals at input A. Despite the disruptive noises, boundary signals still show coherent representation of the edge signals. (C) Output of the model without parameter change. The model does not show much of noise suppression property. (D) Output of the model with a smaller gating parameter (ε = 20). With a smaller gating parameter, the model shows noise suppression property. See the text for further discussion.

Swaminathan, 2004; Raizada & Grossberg, 2003). The new proposal implies that both boundary completion and surface filling-in may be accomplished by long-range connections, presumably within the parallel boundary and surface processing streams that are projections of interblobs and blobs, respectively. The boundary-gating mechanism, by selectively allowing communication between only certain connections, dynamically restructures cell receptive fields. One possible mechanism is axo-axonal gating mechanism of horizontal connections, which is consistent with the report by Kobayashi et al. (2000) of norepinephrine-mediated suppression of horizontal propagation in V1. The new model mechanism runs at least 1000 times faster than previous nearest-neighbor-based diffusion models, and thus clarifies how filling-in can occur with realistic delays. For example, 10 iterations of the non-diffusive filling-in process were used to generate the filled-in image of the Craik-O'Brien-Cornsweet effect in Figure 16B. With nearest-neighbor diffusion, about 10,000 iterations were needed. A simulation using long-range diffusion with interactions beyond nearest-neighbors needed 100 iterations.

A long-range filling-in mechanism has also been proposed by Sepp and Neumann (1999). However, instead of the inter-scale competition used in their model, where different scales compete to gain control to fill a given area, the current mechanism uses boundary signals to dynamically reconfigure the shape of the filling-in areas. Our current approach is intrinsically faster because it does not use inter-scale competition, and eliminates the possibility of blurring caused by imperfect scale selection for a given area in the Sepp-Neumann model. Another approach to parallel filling-in was made by Fischl and Schwartz (1997) who used an approximate solution of a nonlinear convolution. The current mechanism distinguishes itself by combining convolution type filling-in with a direct gating mechanism by boundary signals. The parallel diffusion mechanism of the model is a generalization of the boundary-gated diffusive filling-in model of Grossberg and Todorovic (1988).

Table 2

Names	Symbols	Values
Upper bound of gain control at photoreceptor	B_z	500
Small-time scale input contribution rate for gain control	C_I	200
Large-time scale input contribution rate for gain control	$C_{\bar{I}}$	600
HC feedback constant	B_h	0.04
Photoreceptor depolarization constant	B_s	(B_z / C_I)
Saturation amplitude	a_H	6
Half-way cut-off	b_H	0.1
Shift of permeability of HC gap junction	β_p	0.08
Steepness of permeability of HC gap junction	λ_p	0.01
Size of connected neighbor for horizontal cell	ε_H	8
Activation decay	A	0.5
Depolarization constant	B	1
Hyperpolarization constant	D	1
Center spatial scale for the center-surround stage	α	0.2
Surround spatial scales, small, medium	β	3 (for small scale), 14 (for medium scale)
Amplitude of Gaussian kernel	κ	4
Vertical, horizontal widths of the ON, OFF elliptic simple cell receptive fields	γ_v, γ_h	0.1, $5\gamma_v$,
The shift of the centers of the ON, OFF elliptic simple cell receptive fields	$Shift_{(L)}$, $Shift_{(R)}$	$-\gamma_v$, γ_v
Amplitude of activation function	a_B	0.7
Half-way cut-off of activation function	b_B	0.15
Vertical/horizontal width of the complex cell's gating field	γ_{cv}, γ_{ch}	0.3, 0.7
Small, Medium, Large Scale Weight	w_s , w_m, w_l	0.25, 0.25, 0.5
Baseline bias of multiple-scale input	b_M	0.01
Spatial constant of the cable of the filling-in unit	σ	30 (non-diffusive propagation), 11.2 (long-range diffusion)
Gating constant	ε	100 (non-diffusive propagation), 200 (long-range diffusion)
Amplitude of conductance	δ	given in equation A43 (non-diffusive propagation), 0.6 (long-range diffusion)

4.5 Lightness Anchoring. The model assumes that lightness anchoring happens after surface filling-in occurs in V2 or V4. Within the larger FACADE theory of 3D vision and figure-ground separation (Grossberg, 1994), this allows surface representations at different depths to have their own anchors. Within FACADE, V4 is the area where modal, or visible, 3D surfaces are represented, whereas V2 can fill-in amodal surface representations. The electrophysiological experiment by MacEvoy and Paradiso (2001) reported lightness constancy in V1. However, their experiment does not provide unequivocal evidence that V1 is the place where anchoring occurs. It demonstrates just one aspect of lightness perception; namely, discounting the illuminant, or input normalization, which can be initiated at the earlier model Retinal Adaptation and Contrast stages. Another factor suggesting that anchoring occurs no earlier than V2 is that long-range perceptual grouping, or boundary completion, takes place in V2 (von der Heydt, Peterhans & Baumgartner 1984; Peterhans & von der Heydt, 1989), and influences what surfaces get filled-in; see Gilchrist et. al. (1999) and Grossberg (1994) for further discussion. Extrastriate involvement in lightness anchoring is also suggested by the fact that global integration of information, which is needed for the BHCAW rule, needs a bigger scale of interaction than that supported by horizontal connections in V1 (Angelucci et al., 2002). V2 provides a rich environment for the boundary system (interstripes) and luminance and contrast signals (thin stripes) to interact (Roe and Ts'o, 1995) to begin to form surface percepts. The data of Hung et al. (2001) showing a prominent Craik-O'Brien-Cornsweet effect in V2 are also compatible with this assumption.

4.6 Area Effect in Natural Images. The area effect is limited to simple Ganzfeld configurations. Gilchrist et al. (1999. p. 802) note: "Strictly speaking, the rule applies to visual fields composed of only two regions of nonzero luminance. Application of the rule to more complex images remains to be studied." In the model, it is assumed that when this Ganzfeld configuration was tested, the visual system of the subject adapted its multiple scales to compensate for the unusually sparse visual cues. Sections 2.2 and 4.2 noted that the model incorporates multiple spatial scales which suppress signals that are uniform with respect to each scale. Hence, given the sparse contrasts in the Ganzfeld display, the model would suppress small scales. Multiple scales were not used in the anchoring module, for simplicity. Instead, two different parameter sets were used to explain the area rule: For simple images having just two regions of non-zero luminance (Figure 7), a bigger Gaussian kernel was used. For the other, more complex, images with smaller regions, a smaller kernel was applied. See Table 2 for parameters. The two anchoring kernel sizes were chosen that best fit the data suggested in the Anchoring theory by Gilchrist et al. (1999). Automatic rescaling of anchoring will be incorporated when the model fully exploits its multiple scales for purposes of 3D vision and figure-ground perception, in an extension of how multiple scales have already been used to explain related data in FACADE theory (Grossberg, 1994, 1997; Kelly & Grossberg, 2000).

APPENDIX A: MODEL EQUATIONS

The model implements 2-D simulations on a 200 x 200 grid to represents the visual field.

Retinal adaptation

The potential s_{ij} at position (i, j) of the outer segment of the retinal photoreceptor is simulated by the equation:

$$s_{ij}(t) = I_{ij} \cdot z_{ij}(t), \tag{A1}$$

where I_{ij} is the input and $z_{ij}(t)$ is an automatic gain control term simulating negative feedback mediated by Ca^{2+} ions, among others:

$$\frac{dz_{ij}}{dt} = (B_z - z_{ij}) - z_{ij}\left(C_I I_{ij} + C_{\bar{I}}\bar{I}\right), \tag{A2}$$

(cf., Carpenter and Grossberg, 1981; Grossberg 1980). In (A2), parameter B_z is the asymptote which $z_{ij}(t)$ approaches in the absence of input, and term $-z_{ij}(C_I I_{ij} + C_{\bar{I}}\bar{I}_{ij})$ describes the inactivation of z_{ij} by the present input I_{ij} and a spatial average $\bar{I}$ of all inputs that approximates the effect of recent image scanning by sequences of eye movements. The equilibrium response s_{ij} directly follows from (A1) and (A2):

$$s_{ij} = \frac{B_z I_{ij}}{1 + C_I I_{ij} + C_{\bar{I}}\bar{I}}, \tag{A3}$$

The inner segment of the photoreceptor receives the signal s_{ij} from the outer segment and also gets feedback H_{ij} from the horizontal cell (HC) at position (i, j), as in Figure 10. HC modulation of the output of the inner segment of the photoreceptor is modeled by the equation:

$$S_{ij} = \frac{s_{ij}}{B_h \exp\left(H_{ij}\right) \cdot \left(B_s - s_{ij}\right) + 1}, \tag{A4}$$

where B_h is a small constant, and B_s is a constant close to the value (B_z / C_I). When B_s equals the value of (B_z/C_I), perfect shifts of $\log(I_{ij})$ - S_{ij} curve occur with varying H_{ij} (Figure A1A). When B_s deviates from (B_z/ C_I), compression occurs when $B_s > (B_z/ C_I)$ (Figure A1C). Expansion occurs when $B_s < (B_z/ C_I)$ in addition to the shift. Thus to prevent expansion, which would mean excitation by the HC negative feedback, B_s needs to be bigger or equal to (B_z/ C_I). Figure A2 shows the 10-Mondrian Articulation situation (see Figure 5) with two values for B_s, one equals to (B_z/ C_I), and the other to $1.2(B_z/ C_I)$. This simulation demonstrates that the model is robust under this variation. Compare Figure A2 with the graph in Figure 5G.

The equation (A4) can be generalized as follows.

$$S_{ij} = \frac{s_{ij}}{f(H_{ij}) \cdot \left(B_s - s_{ij}\right) + 1} \ . \tag{A4'}$$

Many increasing functions $f(H_{ij})$ will generate the shift property of S_{ij} as a function of $\log(I_{ij})$. Function $f(H_{ij}) = B_h\exp(H_{ij})$ was chosen because $\exp(H_{ij})$ makes the sensitivity curve shift in an accelerating

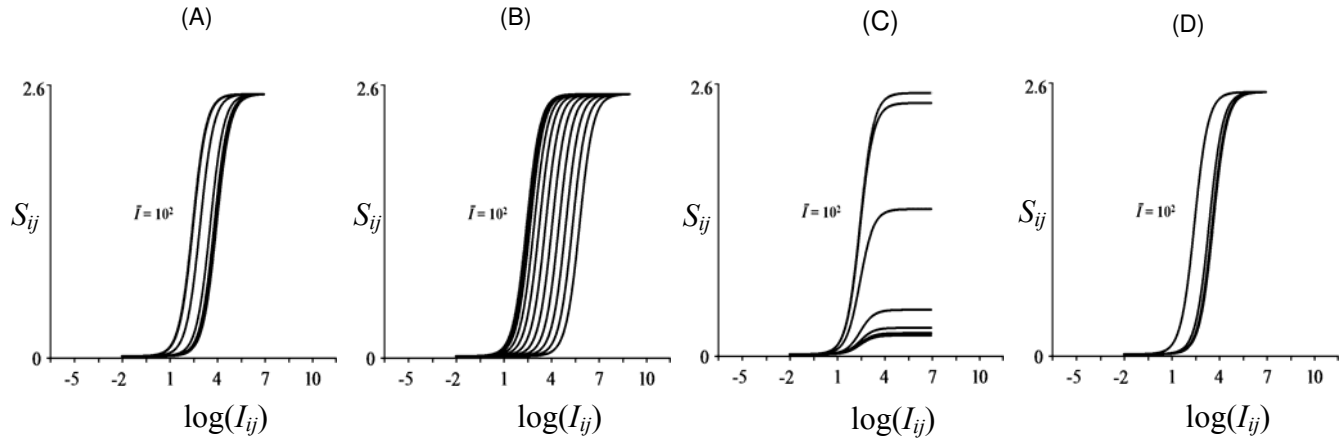

Figure A1. Shift property of spatial contrast adaptation. (A) Shift property of spatial contrast adaptation of the model. The graph shows an example where the $\log(I_{ij})$ - S_{ij} curve smoothly accelerates initially and later decelerates with growing h_{ij}. These curves are generated using the equation A4. These curves and all the following curves in B-D have the same average luminance $\bar{I} = 10^2$. The curves from the left to right have h_{ij} values of 0 to 0.5 with increment 0.1. The same is true for C and D. (B) Shift property with $H_{ij} = h_{ij}$ in placed of the equation A5. The curves show no deceleration. The curves from the left to right have h_{ij} values of 0 to 10 with increment 1. (C) Shift property with no $(B_s - s_{ij})$ term in equation A4. The curves show a prominent compression. (D) Shift property with $f(H_{ij}) = H_{ij}$ in equation A4'. The curves do not have the smooth acceleration shown in graph A.

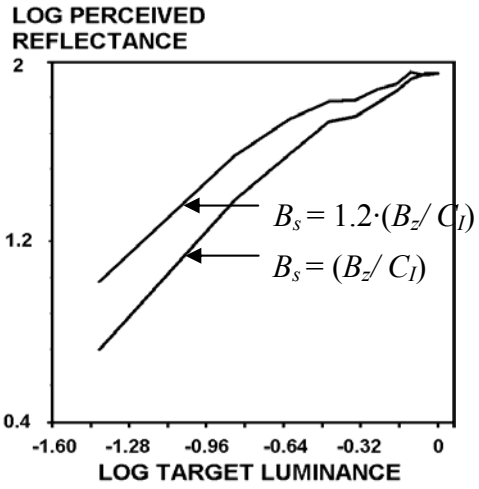

Figure A2. The curves show ten-Mondrian Articulation situation with two values for B_s, one (B_z / C_I), the other $1.2(B_z / C_I)$. While the deviation of 20% from the optimal value shows a bit of compression, the overall quality of Articulation effect remains robust. This demonstrates that the model tolerates a fair amount of fluctuation in the value of the parameter.

manner with increasing H_{ij}, where H_{ij} is the sigmoid output of the HC at (i, j) in response to its potential h_{ij}:

$$H_{ij} = \frac{a_H h_{ij}^2}{b_H^2 + h_{ij}^2}, \qquad \text{(A5)}$$

where a_H and b_H are constants. This bounded function causes the amount of shift to decrease as h_{ij} becomes large. The combination of the initial acceleration by the exponential function in the equation

(A4) and the later saturation by the equation (A5) causes the S_{ij} curve to accelerate initially and later decelerate with increasing h_{ij}. Figure (A1A) shows an example of this shift property. The leftmost curve represents the S_{ij} curve with $h_{ij} = 0$; the other curves have h_{ij} values of 0.1, 0.2,… , 0.5, respectively. All these curves have the same average luminance $\bar{I} = 10^2$. The shift property is generated at any average luminance $\bar{I}$. Note that the leftmost curve in Figure (A1A) is the same as the curve with $\bar{I} = 10^2$ in Figure 2C. Figure (A1B) shows what happens when $H_{ij} = h_{ij}$ is used in stead of equation (A5), with all other equations the same; it shows no deceleration. Here, h_{ij} values of 0 to 10 were used with increments of 1. Figure (A1C) shows a situation where the term $(B_s - s_{ij})$ in equation A4 has been replaced by 1; it shows a prominent compression. For this simulation, h_{ij} values of 0 to 0.5 with increments of 0.1 were used. Figure (A1D) shows a situation with $f(H_{ij}) = H_{ij}$ in equation A4'; it does not have the smooth acceleration shown in Figure (A1A). The same h_{ij} values as for Figure (A1C) were used for this simulation.

The potential of an HC connected to its neighbors through gap junctions is defined as follows.

$$\frac{dh_{ij}}{dt} = -h_{ij} + \sum_{(p,q)\in N_{ij}^H} P_{pqij}(h_{pq} - h_{ij}) + S_{ij}, \qquad \text{(A6)}$$

where P_{pqij} is the permeability between cells at (i, j) and (p, q); namely,

$$P_{pqij} = \frac{-1}{1 + \exp[-(|S_{ij} - S_{pq}| - \beta_p)/\lambda_p]} + 1 \qquad \text{(A7)}$$

Terms β_p and λ_p in (A7) are constants, and $N^H{}_{ij}$ in (A6) is the neighborhood of size ε_H to which the model HC at (i, j) is connected:

$$N_{ij}^H = \left\{(p,q) : \sqrt{(i-p)^2 + (j-q)^2} \le \varepsilon_H \text{ and } (p,q) \ne (i,j)\right\} \qquad \text{(A8)}$$

Center - Surround Stage

The retinally adapted signal S_{ij} is then processed by small-scale and medium-scale on-center off-surround and off-center on-surround networks. In the following, scale subscripts (e.g., x_s and x_m for small and medium scales, respectively) are omitted for simplicity. An on-center off-surround (ON) network of cell activities $x^+{}_{ij}$ that obey membrane equations is defined as follows:

$$\frac{dx_{ij}^+}{dt} = -Ax_{ij}^+ + (B - x_{ij}^+)C_{ij} - (x_{ij}^+ + D)E_{ij}, \qquad \text{(A9)}$$

where A, B and D are constants. The on-center input obeys:

$$C_{ij} = \left(\sum_{(p,q)\in N_{ij}^C} S_{pq} C_{pqij}\right) \frac{W_C}{\sum_{(p,q)\in N_{ij}^C} C_{pqij}}, \qquad \text{(A10)}$$

and the off-surround input obeys:

$$E_{ij} = \left(\sum_{(p,q)\in N_{ij}^E} S_{pq} E_{pqij}\right) \frac{W_E}{\sum_{(p,q)\in N_{ij}^E} E_{pqij}}, \qquad \text{(A11)}$$

with the excitatory Gaussian on-center kernel:

$$C_{pqij} = C\exp\left\{-\frac{(p-i)^2+(q-j)^2}{\alpha^2}\right\} \quad \text{(A12)}$$

and the inhibitory Gaussian off-surround kernel:

$$E_{pqij} = E\exp\left\{-\frac{(p-i)^2+(q-j)^2}{\beta^2}\right\}. \quad \text{(A13)}$$

Coefficients C and E in (A12) and (A13), which normalize and make the sums of the center and surround kernels the same, are defined by:

$$C = \frac{W_C}{\sum_{(p,q)\in N^C}\exp\left\{-\frac{p^2+q^2}{\alpha^2}\right\}} \quad \text{(A14)}$$

and

$$E = \frac{W_E}{\sum_{(p,q)\in N^E}\exp\left\{-\frac{p^2+q^2}{\beta^2}\right\}}\ . \quad \text{(A15)}$$

Terms α, β, W_C and W_E are constants. N^C_{ij} in equation (A10) is the on-center neighborhood to which the cell at (i, j) is connected:

$$N^C_{ij} = \left\{(p,q) : \sqrt{(i-p)^2+(j-q)^2} \le \varepsilon_C \text{ and } 0 \le p \le 199 \text{ and } 0 \le q \le 199\right\}, \quad \text{(A16)}$$

where ε_C is a constant defining the size of the neighbor. N^C in equation (A14) is the neighbor for the standard center kernel defined as follows.

$$N^C = \left\{(p,q) : \sqrt{(i-p)^2+(j-q)^2} \le \varepsilon_C\right\}. \quad \text{(A17)}$$

The only difference between N^C_{ij} and N^C is that N^C_{ij} is constrained by the boundary of the image (200x200), which may cut kernels along the borders, while N^C, which defines the whole kernel, is not. For brevity, the same convention between N^C_{ij} and N^C is used for other equations as well. For example, N^E_{ij} in equation (A11) is the neighborhood for the surround kernel with a size ε_E with the same form of definition as equation (A16), and its corresponding standard neighbor is N^E with the same form of definition as equation (A17). See Table 1 for parameters.

For each position, the normalizing factors W_C / ΣC_{pqij} and W_E / ΣE_{pqij} in (A10) and (A11) are constants, mostly just 1, except for the positions along the border of the image. Normalization eliminates unwanted boundary effects created by filters with a fixed kernel size. In case of a center-surround filter, for example, without normalization, halos along the border of the image can occur because of the disinhibition caused by cut kernels there.

The equilibrium activities of (A9) are:

$$x^+_{ij} = \frac{BC_{ij} - DE_{ij}}{A + C_{ij} + E_{ij}}. \quad \text{(A18)}$$

The corresponding equilibrium activities of the off-center on-surround (OFF) network are:

$$x_{ij}^{-} = \frac{BC_{ij}^{-} - DE_{ij}^{-}}{A + C_{ij}^{-} + E_{ij}^{-}} \tag{A19}$$

In (A19),

$$C_{ij}^{-} = E_{ij} \tag{A20}$$

and

$$E_{ij}^{-} = C_{ij} \tag{A21}$$

(Grossberg, Mingolla, and Williamson, 1995). The output signals are rectified versions of x_{ij}^{+} and x_{ij}^{-}:

$$X_{ij}^{+} = \left[x_{ij}^{+}\right]^{+} \tag{A22}$$

and

$$X_{ij}^{-} = \left[x_{ij}^{-}\right]^{+}. \tag{A23}$$

Luminance signals L_{ij}, which constitute the large-scale of the center-surround process, are defined by:

$$L_{ij} = S_{ij} \tag{A24}$$

Through these processes, the initial stage of the model achieves automatic gain control in all its small, medium and large scales.

Boundary System

Simple cell activities are simulated using a network of units having polarized and oriented receptive fields around a gird of pixel units. Figure (A3A) shows pixel units at (i, j) denoted as small filled circles, and eight surrounding numbered positions at (i', j') where pairs of model simple cells with the same orientation but opposite contrast polarity are located. Each simple cell is represented by a half-filled and half-hollow oriented ellipse (Figure A3B). The eight positions are as follows: (i + 0.5, j), (i + 0.5, j + 0.5), (i, j + 0.5), (i − 0.5, j + 0.5), (i − 0.5, j), (i − 0.5, j − 0.5), (i, j − 0.5), (i + 0.5, j − 0.5). A pair of simulated simple cells has one of 4 orientations: (0, π/4, π/2, 3π/4). The even numbered positions have only two (0, π/2) orientations; positions 3 and 7 have three orientations (0, π/4, 3π/4); and positions 1 and 5 have three orientations (π/4, π/2, 3π/4). The responses of simple cells are modeled using medium-scale contrast signals. This simplification was chosen because it gives relative clean edge signals. The outputs from simple cells having light-dark and dark-light luminance polarities in their receptive fields are simulated as follows:

$$s_{i'j'k}^{LD} = \left[\left(L_{i'j'k}^{+} + R_{i'j'k}^{-}\right) - \left(R_{i'j'k}^{+} + L_{i'j'k}^{-}\right)\right]^{+} \tag{A25}$$

$$s_{i'j'k}^{DL} = \left[\left(R_{i'j'k}^{+} + L_{i'j'k}^{-}\right) - \left(L_{i'j'k}^{+} + R_{i'j'k}^{-}\right)\right]^{+}, \tag{A26}$$

where the superscripts *LD* and *DL* indicate light-dark and dark-light luminance polarities of the model simple cell receptive fields, respectively, and k denotes the orientation. Activation of a model simple cell left and right sub-receptive fields from ON and OFF channels is modeled as follows:

$$L^{+}_{i'j'k} = \left(\sum_{(p,q)\in N^{B}_{i'j'}} X^{m+}_{pq} G_{pqi'j',kL} \right) \frac{W_B}{\sum_{(p,q)\in N^{B}_{i'j'}} G_{pqi'j',k}} \tag{A27}$$

$$R^{+}_{i'j'k} = \left(\sum_{(p,q)\in N^{B}_{i'j'}} X^{m+}_{pq} G_{pqi'j',kR} \right) \frac{W_B}{\sum_{(p,q)\in N^{B}_{i'j'}} G_{pqi'j',k}} \tag{A28}$$

and

$$L^{-}_{i'j'} = \left(\sum_{(p,q)\in N^{B}_{i'j'}} X^{m-}_{pq} G_{pqi'j',kL} \right) \frac{W_B}{\sum_{(p,q)\in N^{B}_{i'j'}} G_{pqi'j',k}} \tag{A29}$$

$$R^{-}_{i'j'} = \left(\sum_{(p,q)\in N^{B}_{i'j'}} X^{m-}_{pq} G_{pqi'j',kR} \right) \frac{W_B}{\sum_{(p,q)\in N^{B}_{i'j'}} G_{pqi'j',k}} . \tag{A30}$$

Subscripts L and R indicate the two sub-receptive fields for the simple cell with L indicating the left part (to the anticlockwise) of the sub-receptive field, and the R the right part (to the clockwise) of the sub-receptive field along the axis of the orientation. Constant W_B is the sum of the standard kernel weights of the simple cell:

$$W_B = \sum_{(p,q)\in N^{B}} G_{pqi'j',k} , \tag{A31}$$

At each position, the normalization factor W_B / $\Sigma G_{pqi'j'k}$ is constant, mostly just 1, except for positions along the border of the image where the Gaussian kernel is incomplete. To see the size of the simple cell kernel neighbor, N^B, see ε_B in Table 1.

A pair of oriented Gaussian kernels, indicated as L and R, simulates receptive fields for the simple cell:

$$G_{pqi'j',k,(L\,or\,R)} = \kappa \exp\left\{ - \frac{\left[(p-i')\cos(\pi k/4) + (q-j')\sin(\pi k/4) \right]^2}{\gamma_h^2} - \frac{\left[-(p-i')\sin(\pi k/4) + (q-j')\cos(\pi k/4) + Shift_{(L\,or\,R)} \right]^2}{\gamma_v^2} \right\}, \tag{A32}$$

where $Shift_{(L)}$ and $Shift_{(R)}$, which shift the sub-fields orthogonal to the axis of orientation, are constants $-\gamma_v$ and γ_v, respectively; κ is a constant. k is one of the four numbers (1, 2, 3, 4) that sets the orientation; and γ_h and γ_v are constants that define the widths of the kernel along and across the axis of orientation, respectively.

The model complex cells are also located at the eight (i', j') positions, and have oriented receptive fields, as illustrated in Figure (A3C). The model complex cell of orientation k at (i', j') pools the outputs of a pair of simple cells as follows:

$$z_{i'j'k} = s^{LD}_{i'j'k} + s^{DL}_{i'j'k} . \tag{A33}$$

This cell potential goes through an activation function:

$$Z_{i'j'k} = f(z_{i'j'k}), \tag{A34}$$

where

$$f(x) = \frac{a_B x^{1.7}}{b_B^2 + x^{1.7}}. \tag{A35}$$

The parameter 1.7 of the power of x was in (A35) used that gave the optimal strength of the boundary signals across simulations. A gradual degradation of image quality occurs as the parameter deviates from the optimal value (data not shown). The complex cell gates any horizontal connections that cross its gating field. The effective gating strength at a point (x, y) along a passing horizontal connection is the product of the gating weight ($G^c_{xyi'j'k}$) at the point and the activation of the gating complex cell at (i', j') ($Z_{i'j'k}$):

$$Z'_{xyi'j'k} = G^c_{xyi'j'k} Z_{i'j'k}, \tag{A36}$$

where x, y are continuous variables. The Gaussian kernel of the gating field, which represents the spatial spread of gating weight of complex cell axons at points (x, y) along the line (i, j) - (p, q), is defined as follows:

$$G^c_{xyi'j'k} = \exp\left\{ -\frac{\left[(x-i')\cos(\pi k/4) + (y-j')\sin(\pi k/4)\right]^2}{\gamma_{ch}^2} - \frac{\left[-(x-i')\sin(\pi k/4) + (y-j')\cos(\pi k/4)\right]^2}{\gamma_{cv}^2} \right\}, \tag{A37}$$

Figures (A3D) and (A3E) show an example of the complex cell gating mechanism for a given input. For a given complex gating field, it is assumed that the gating occurs at just one point for each crossing connection. The gating point (x, y), which lies along the line (i, j) - (p, q), is chosen that gives the maximum value of equation (A37). In the simulation, 10 equidistance points along the cross-section between the ellipse and the crossing line (i, j) - (p, q) were examined to find the approximate inflection (maximum) point as shown in Figure (A3F). The size of each dot in the figure represents the value $G^c_{xyi'j'k}$ of equation (A37) for each examined point.

Filling-in

Cortical filling-in is driven by the inputs M_{ij} which are the pooled luminance and contrast signals as follows:

$$M_{ij} = \left[w_s \left(X_{ij}^{s+} - X_{ij}^{s-} \right) + w_m \left(X_{ij}^{m+} - X_{ij}^{m-} \right) + w_l L_{ij} + b_M \right]^+, \tag{A38}$$

where w_s, w_m, w_l, are weighting constants, and b_M is a tonic bias term. Either of two versions of the filling-in process yield equivalent simulations of the targeted data. A long-range diffusion process, much as in the retinal HC diffusion in (A6), works well with activities F_{ij} instead of the activities h_{ij} in (A6), and inputs M_{ij} instead of the inputs S_{ij} in (A6). This long-range diffusion runs 100 times faster than previous nearest-neighbor diffusions for filling-in. In addition, the conductance P_{pqij} are divisively gated by activated complex cells along its path. They are defined by:

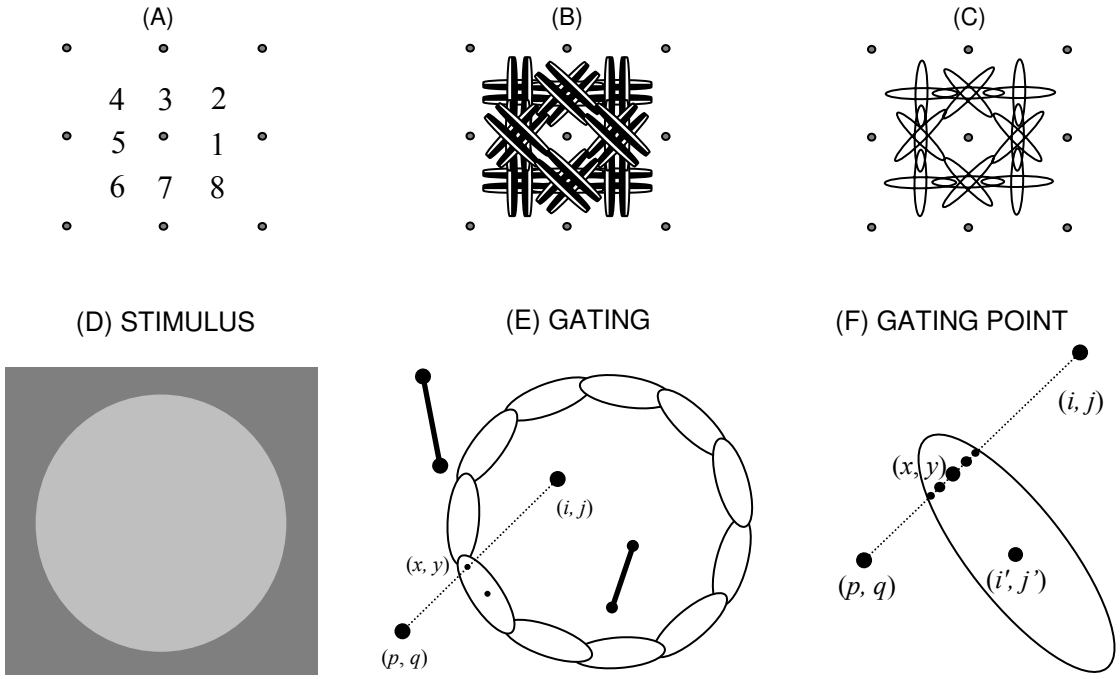

Figure A3. Model boundary system and gating mechanism. (A) Relative positions of model simple and complex cells to pixel points. The model simple and complex cells are poisoned between the pixel points. For example, for a given pixel in the middle (the small gray filled circle in the middle), there are eight surrounding positions (1 through 8) where simple and complex cells are placed. (B) Configuration of simple cell network around a pixel unit in the middle. (C) Gating field of complex cells around the pixel unit. Just one set of pixel-complex and simple cell relationship is shown for clarity. The same pixel-complex and simple cell relationship applies to other pixels. (D) Example of a stimulus. (E) Illustration of gating mechanism for stimulus D. It illustrates the resulting activations of gating components with the input in figure D. The activated complex cells that surround the disk area gate any connections crossing their gating fields represented as ellipses. The connection between (i, j) and (p, q) is gated (the doted line) by a gating signal at (x, y) in the gating field of the complex cell centered at (i', j'). The other connections are not gated, being allowed to have high conductances (solid lines). For the purpose of illustration, more orientations are shown than the four orientations used for the simulations. (F) Position of the gating point. The figure shows the blown up part of the gated part of the connection in the figure E. In the simulation, 10 equidistance points (5 of them are shown for clarity) along the cross-section between the ellipse and the crossing line (i, j) - (p, q) were examined to find the approximate inflection (maximum) point. The size of each dot represents the value $G^{c}_{xyi'j'k}$ of equation (A37) for each examined point.

$$P_{pqij} = \frac{\delta \exp\left[-\left((i-p)^2 + (j-q)^2\right)/\sigma^2\right]}{\prod_{i'j'k}\left(1+\varepsilon Z'_{i'j'k}\right)}, \qquad \text{(A39)}$$

where σ, δ and ε are constants. The numerator of (A39) describes the strengths of horizontal connections, assumed to have a Gaussian distribution, such that longer connections have smaller strengths.

Alternatively, a long-range propagation process that does not require diffusion, but is normalized in a different way, generates essentially identical simulations, which are the ones that are shown in this article. This process runs 1000 times faster than nearest-neighbor diffusion processes. The first step of the filling-in is to activate the filling-in units with the pooled multiple-scale input signals M_{ij}:

$$F_{ij} = M_{ij} \,. \tag{A40}$$

Here, the filling-in activity F_{ij} (t+1) equals:

$$F_{ij}(t+1) = \left(\sum_{(p,q)\in N_{ij}^F} F_{pq}(t) P_{pqij} \right) \frac{W_F}{\sum_{(p,q)\in N_{ij}^F} P_{pqij}}, \tag{A41}$$

where the conductance P_{pqij} shares the same form of equation (A39) with different parameters (see Table 2). The constant W_F in (A41) is a sum of conductances defined as follows:

$$W_F = \sum_{(p,q)\in N^F} \delta \exp\left[-\left(i^2 + j^2 \right) / \sigma_F^2 \right]. \tag{A42}$$

Since W_F is constant, the constant δ for a fixed σ is calculated as follows:

$$\delta = \frac{W_F}{\sum_{(p,q)\in N^F} \exp\left\{ -\left(i^2 + j^2 \right) / \sigma^2 \right\}} \,. \tag{A43}$$

The size of the filling-in neighborhood N^F is determined by parameter ε_F in Table 1. Equation (A41) assumes that the filling-in unit can normalize its conductances. The normalizing factor $W_F/\Sigma P_{pqij}$ affects the conductance in two ways. First, at the border of the image, the incomplete kernels get normalized to have the same size as W_F. Second, normalization compensates for the overall lost conductance caused by gating (division by the denominator in equation (A39)). By this normalization process, the sum of the effective conductances equals:

$$W_F = \sum_{pq} \left(P_{pqij} \frac{W_F}{\sum_{pq} P_{pqij}} \right) \,. \tag{A44}$$

For example, if half of the input connections were totally blocked by gating signals, the unit would try to increase the effective input flow by doubling the efficacy of the remaining connections, keeping the sum of all the incoming conductances the same. Ten iterations of equation (A41) gives satisfactory filled-in results.

Lightness Anchoring

At the anchoring stage, the filled-in surface activity F_{ij} becomes anchored into the activity A_{ij} using the following equation:

$$\frac{dA_{ij}}{dt} = -B_A A_{ij} + \Psi\left(C_A - A_{ij} \right) F_{ij}, \tag{A45}$$

where B_A and C_A are constants. The tonic gain control signal Ψ, which modulates all the anchoring activities A_{ij}, uses the following equation.

$$\frac{d\Psi}{dt} = \tau_\Psi \left\{ -\Psi + \left(B_\Psi - \Psi \right) T_\Psi - \Psi H \right\}. \tag{A46}$$

The term τ_Ψ is a time constant that determines the speed of integration of equation (A46). The term $-\Psi$ is a leakage component. The next term $(B_\Psi - \Psi)T_\Psi$ is an excitatory component that drives the gain control

signal Ψ toward its maximum B_Ψ until the inhibitory component ΨH kicks in due to the activation of the suppressive signal H, which is defined as follows:

$$\frac{dH}{dt} = \tau_H \left\{ -H + (\varphi - H) \sum_{ij} B_{ij} \right\}, \tag{A47}$$

where τ_H is a time constant. Using the equation (A47), the suppressive signal H quickly becomes activated and suppresses the gain control activity Ψ whenever there is an activated output cell at the BHCAW module, which signals the anchoring of blurred "highest luminance" to white. The output of the BHCAW module B_{ij} is defined as follows:

$$B_{ij} = f^B(b_{ij}), \tag{A48}$$

where the signal function $f^B(x)$ is a steep sigmoid:

$$f^B(x) = \frac{x^m}{\varpi^m + x^m}, \tag{A49}$$

where m and ϖ are constants; see Table 3. Function b_{ij} in (A48) is a blurred version of the anchoring signal A_{ij}:

$$b_{ij} = \sum_{(p,q) \in N_{ij}^A} G_{pqij}^A A_{pq}, \tag{A50}$$

where the blurring Gaussian anchoring kernel is defined by:

$$G_{pqij}^A = G^A \exp\left\{ -\frac{(p-i)^2 + (q-j)^2}{\varsigma_A^2} \right\} \frac{W_A}{\sum_{(p,q) \in N_{ij}^A} G_{pqij}^A}, \tag{A51}$$

where constant

$$G^A = \frac{W_A}{\sum_{(p,q) \in N^A} \exp\left\{ -\frac{p^2 + q^2}{\zeta_A^2} \right\}}, \tag{A52}$$

and W_A and ζ_A are constants. The size of the blurring neighborhood N^A is determined by paramenter ε_A in Table 1. When m in equation (A49) is large, H approximates a step function

$$\begin{cases} H = \varphi & \text{whenever any } b_{ij} \geq \varpi \\ H = 0 & \text{otherwise,} \end{cases} \tag{A53}$$

where φ is a constant. In the simulation, equation (A53) was used in place of equations (A47) to (A49).

Table 3

Names	Symbols	Values
Decay rate for Anchoring	B_A	1
Depolarization constant for Anchoring	C_A	10
Time constant of modulatory unit of anchoring	τ_Ψ	0.01
Depolarization constant of modulatory unit of anchoring	B_Ψ	1.3
Recharge rate of tonic activity	T_Ψ	1
Power of BHCAW activation function	m	100
White	ϖ	0.5
Hyperpolarization constant for gain control	φ	8
Spatial scale for Anchoring	ζ_A	100 (for the area rule), 4 (for the others)
Size of connection range for the center of center-surround unit	ε_C	6 (for small scale), 28 (for medium scale)
Size of connection range for the surround of center-surround unit	ε_E	6 (for small scale), 28 (for medium scale)
Size of connection range for the half kernel of simple cell	ε_B	3
Size of connection range for the blurring kernel of Anchoring	ε_A	100 (for the area rule), 4 (for the others)
Size of connection range for the filling-in unit	ε_F	8
Sizes of various standard kernels	W_C, W_E, W_B, W_A, W_F	0.6, 0.6, 4, 1, 1

APPENDIX B

To generate the stimuli with different background luminance (Figure 2C), the following formula was used:

$$I_{ij} = \rho_{ij} E_{ij}, \qquad \text{(B1)}$$

where I_{ij} is the luminance at point (i, j), ρ_{ij} is the reflectance at point (i, j), and E_{ij} is the illumination on point (i, j) (Hurlbert, 1989). For a given stimulus, E_{ij} was uniform across the image. For practical purposes, ρ_{ij} in equation (B1) was replaced by the luminance at point (i, j) of the original image. This situation is roughly equivalent to a viewing situation where a picture is exposed to uniform background illumination. The range of ρ_{ij} was chosen to be –4 to 5 in log-scale for a fixed illumination level to examine the full dynamic profile of the shift property. See Figure 2C for the values of illumination E_{ij} used for the simulations.

References

Adams, M.M., Hof, P.R., Gattass, R., Webster, M.J., & Ungerleider, L.G. (2000). Visual cortical projections and chemoarchitecture of macaque monkey pulvinar. *Journal of Comparative Neurology*, **419**, 377-393.

Adelson, E.H., & Pentland, A.P. (1996). The perception of shading and reflectance. In D.C. Knill & W. Richards (Eds.), *Perception as Bayesian inference* (pp. 409-423). New York: Cambridge University Press.

Adelson, E.H. (2000). Lightness perception and lightness illusions. In *The Cognitive Neurosciences*, Ed., M. Gazzaniga (Cambridge, MA: MIT Press), pp 339-351.

Alonso, J.M., & Martinez, L.M. (1998). Functional connectivity between simple cells and complex cells in cat striate cortex. *Nature Neuroscience*, **1**, 395-403.

Alonso, J.M., Usrey, W.M., & Reid, R.C. (2001). Rules of connectivity between geniculate cells and simple cells in cat primary visual cortex. *Journal of Neuroscience*, **21**, 4002-4015.

Anderson, B.L. (1997). A theory of illusory lightness and transparency in monocular and binocular images: the role of contour junctions. *Perception*, **26**, 419-453.

Angelucci, A., Levitt, J.B., Walton, E.J., Hupé, J.M., Bullier, J., & Lund, J.S. (2002). Circuits for local and global signal integration in primary visual cortex. *Journal of Neuroscience*, **22**, 8633-8646.

Arend, L.E. (1990). Perceived lightness, but not brightness of achromatic surfaces depends on perceived depth information. *Perception & Psychophysics*, **48**, 82-90.

Arend, L.E. (1993). Mesopic lightness, brightness, and brightness contrast. *Perception & Psychophysics*, **54**, 469-476.

Arend, L.E. (1994). Surface colors, illumination, and surface geometry: Intrinsic-image models of human color perception. In A. Gilchrist (Ed.), *Lightness, brightness, and transparency* (pp. 159-213). Hillsdale, NJ: Erlbaum.

Arend, L.E., & Reeves, A. (1986). Simultaneous color constancy. *Journal of the Optical Society America*, **3**, 1743-1751.

Arend, L.E., & Spehar, B. (1993a). Lightness, brightness, and brightness contrast: 1. Illuminance variation. *Perception & Psychophysics*, **54**, 446-456.

Arend, L.E., & Spehar, B. (1993b). Lightness, brightness, and brightness contrast: 2. Reflectance variation. *Perception & Psychophysics*, **54**, 457-468.

Arrington, K.F. (1994). The temporal dynamics of brightness filling-in. *Vision Research*, **24**, 3371-3387.

Baccus, S.A., & Meister, M. (2002). Fast and slow contrast adaptation in retinal circuitry. *Neuron*, **36**, 909-919.

Barlow, H.B. (1953). Summation and inhibition in the frog's retina. *Journal of Physiology (London)*, **119**, 69-88.

Barlow, H.B., & Levick, W.R. (1969). Three factors limiting the reliable detection of light by retinal ganglion cells of the cat. *Journal of Physiology*, **200**, 1-24.

Barlow, R.B., Snodderly, D.M., & Swadlow, H.A. (1978). Intensity coding in primate visual system. *Experimental Brain Research*, **31**, 163-177.

Bartlett, J.R., & Doty, R.W. (1974). Response of units in striate cortex of squirrel monkeys to visual and electrical stimuli. *Journal of Neurophysiology*, **37**, 621-641.

Baylor, D.A., Hodgkin, A.L., Lamb, T.D. (1974a). The electrical response of turtle cones to flashes and steps of light. *Journal of Physiology*, **242**, 685-727.

Baylor, D.A., Hodgkin, A.L., Lamb, T.D. (1974b). Reconstruction of the electrical responses of turtle cones to flashes and steps of light. *Journal of Physiology*, **242**, 759-791.

Benda, J., Bock, R., Rujan, P., & Ammermuller, J. (2001). Asymmetrical dynamics of voltage spread in retinal horizontal cell networks. *Visulal Neuroscience*, **18**, 835-848.

Bickford, M.E., Günlük, A.E., Guido, W., & Sherman, S.M. (1993). Evidence that cholinergic axons from the parabrachial region of the brainstem are the exclusive source of nitric oxide in the lateral geniculate nucleus of the cat. *Journal of Comparative Neurology*, **334**, 410-430.

Bloomfield, S.A., Xin, D., & Persky, S.E. (1995). A comparison of receptive field and tracer coupling size of horizontal cells in the rabbit retina. *Visual Neuroscience*, **12**, 985-999.

Bonato F, & Cataliotti J. (2000). The effects of figure/ground, perceived area, and target saliency on the luminosity threshold. *Perception & Psychophysics*, **62**, 341-349.

Bonato F, & Gilchrist A.L. (1994). The perception of luminosity on different backgrounds and in different illuminations. *Perception*, **23**, 991-1006.

Bonato F, & Gilchrist A.L. (1999). Perceived area and the luminosity threshold. *Perception & Psychophysics*, **61**, 786-797.

Bressan, P. (2001), Explaining lightness illusions. *Perception*, **30**, 1031-1046.

Bressan, P., Mingolla, E., Spillmann, L., & Watanabe, T. (1997). Neon color spreading: a review. *Perception*, **26**, 1353-1366.

Brown, S.P., & Masland, R.H. (2001). Spatial scale and cellular substrate of contrast adaptation by retinal ganglion cells. *Nature Neuroscience*, **4**, 44-51.

Budd, J.M. (1998). Extrastriate feedback to primary visual cortex in primates: a quantitative analysis of connectivity. *Proceedings of The Royal Society of London Series B-Biological Sciences*, **265**, 1037-1044.

Bullier, J., & Henry, G.H. (1979). Laminar distribution of first-order neurons and afferent terminals in cat striate cortex. *Journal of Neurophysiology*, **42**, 1271-1281.

Bullier, J., Hupé, J.M., James, A.C., & Girard, P. (1996). Functional interactions between areas V1 and V2 in the monkey. *Journal of Physiology Paris*, **90**, 217-220.

Bullier, J., Hupé, J.M., James, A.C., & Girard, P. (2001). The role of feedback connections in shaping the responses of visual cortical neurons. *Progress in Brain Research*, **134**, 193-204.

Burkhardt, D.A. (1994). Light adaptation and photopigment bleaching in cone photoreceptors *in situ* in the retina of the turtle. *Journal of Neuroscience*, **14**, 1091-1105.

Calvert, P.D., Govardovskii, V.I., Arshavsky, V.Y., & Makino, C.L. (2002). Two temporal phases of light adaptation in retinal rods. *Journal of General Physiology*, **119**, 129-145.

Callaway, E.M. (1998). Local circuits in primary visual cortex of the macaque monkey. *Annual Review of Neuroscience,* **21**, 47-74.

Caputo, G. (1998). Texture brightness filling-in. *Vision Research*, **38**, 841-851.

Carpenter G., & Grossberg, S. (1981). Adaptation and transmitter gating in vertebrate photoreceptors. *Journal of Theoretical Neurobiology*, **1**, 1-42.

Cataliotti, J., & Gilchrist, A. (1995). Local and global processes in surface lightness perception. *Perception & Psychophysics*, **57**, 125-135.

Chapman, B., & Gödecke, I. (2002). No ON-OFF maps in supragranular layers of ferret visual cortex. *Journal of Neurophysiology*, **88**, 2163-2166.

Cohen, M.A., & Grossberg, S. (1984). Neural dynamics of brightness perception: features, boundaries, diffusion, and resonance. *Perception & Psychophysics*, **36**, 428-456.

Cole, R.E., & Diamond, A.L., (1971). Amount of surround and test inducing separation in simultaneous brightness contrast. *Perception & Psychophysics*, **9**, 125-128.

Cook, P.B., & McReynolds, J.S. (1998). Lateral inhibition in the inner retina is important for spatial tuning of ganglion cells. *Nature Neuroscience*, **1**, 714-719.

Cornsweet, T.N. (1970). Visual perception. New York: Academic Press.

Dacheux, R.F., & Raviola, E. (1982). Horizontal cells in the retina of the rabbit. *Journal of Neuroscience*, **2**, 1486-1493.

Davey, M.P., Maddess, T., & Srinivasan, M.V., (1998). The spatiotemporal properties of the Craik-O'Brien-Cornsweet effect are consistent with 'filling-in'. *Vision Research*, **38**, 2037-2046.

Davidson, M., & Whiteside, J.A. (1971). Human brightness perception near sharp contours. *Journal of the Optical Society America*, **61**, 530-536.

Demb, J.B. (2002). Multiple mechanisms for contrast adaptation in the retina. *Neuron*, **36**, 781-783.

De Valois, R.L., Cottaris, N.P., Mahon, L.E., Elfar, S.D., & Wilson, J.A., (2000). Spatial and temporal receptive fields of geniculate and cortical cells and directional selectivity. *Vision Research*, **40**, 3685-3702.

De Valois, R.L., & De Valois, K.K. (1988). *Spatial vision*. New York: Oxford University Press.

DeVries, S.H., & Schwartz, E.A. (1989). Modulation of an electrical synapse between solitary pairs of catfish horizontal cells by dopamine and second messengers. *Journal of Physiology*. **414**, 351-375.

DeVries, S.H., & Schwartz, E.A. (1992). Hemi-gap-junction channels in solitary horizontal cells of the catfish retina. *Journal of Physiology*. **445**, 201-230.

Dolan, R.P., & Schiller, P.H. (1994). Effects of ON channel blockade with 2-amino-4-phosphonobutyrate (APB) on brightness and contrast perception in monkeys. *Visual Neuroscience*, **11**, 23-32.

Dowling, J.E. (1987). The Retina: An approachable part of the brain. (Cambridge, MA; Harvard University Press).

Dresp, B., & Grossberg, S. (1997). Contour integration across polarities and spatial gaps: from local contrast filtering to global grouping. *Vision Research*, **37**, 913-924.

Dubin, M.W., & Cleland, B.G. (1977). Organization of visual inputs to interneurons of lateral geniculate nucleus of the cat. *Journal of Neurophysiology*, **40**, 410-427.

Edwards, D.P., Purpura, K.P., & Kaplan, E. (1995). Contrast sensitivity and spatial frequency response of primate cortical neurons in and around the cytochrome oxidase blobs. *Vision Research*, **35**, 1501-1523.

Enroth-Cugell, C., & Shapley, R.M. (1973a). Adaptation and dynamics of cat retinal ganglion cells. *Journal of Physiology*, **233**, 271–309.

Enroth-Cugell, C., & Shapley, R.M. (1973b). Flux, not retinal illumination, is what cat retinal ganglion cells really care about. *Journal of Physiology*, **233**, 311-326.

Erisir, A., Van Horn, S.C., Bickford, M.E., & Sherman, S.M. (1997). Immunocytochemistry and distribution of parabrachial terminals in the lateral geniculate nucleus of the cat: a comparison with corticogeniculate terminal. *Journal of Comparative Neurology*, **377**, 535-549.

Erwin, E., Baker, F.H., Busen, W.F., & Malpeli, J.G. (1999). Relationship between laminar topology and retinotopy in the rhesus lateral geniculate nucleus: results from a functional atlas. *Journal of Comparative Neurology*, **407**, 92-102.

Eysel, U.T., Pape, H.C. & Van Schayck, R. (1986). Excitatory and differential disinhibitory actions of acetylcholine in the lateral geniculate nucleus of the cat. *Journal of Physiology*, **370**, 233-254.

Eysel, U.T., & Schweigart, G. (1999). Increased receptive field size in the surround of chronic lesions in the adult cat visual cortex. *Cerebral Cortex*, **9**, 101-109.

Fahrenfort, I., Habets, R.L., Spekreijse, H., & Kamermans, M. (1999). Intrinsic cone adaptation modulates feedback efficiency from horizontal cells to cones. *Journal of General Physiology*, **114**, 511-24.

Fain, G.L. (2001), Dark adaptation. *Progress in Brain Research*, **131**, 383-394.

Felisberti, F., & Derrington, A.M. (2001). Long-range interactions in the lateral geniculate nucleus of the New-World monkey, Callithrix jacchus. *Visulal Neuroscience*, **18**, 209-218.

Felleman, D.J., & Van Essen, D.C. (1991). Distributed hierarchical processing in the primate cerebral cortex. *Cerebral Cortex*, **1**, 1-47.

Ferster, D., Chung, S., & Wheat, H. (1996). Orientation selectivity of thalamic input to simple cells of cat visual cortex. *Nature*, **380**, 249-252.

Field, D.J., Hayes, A., & Hess, R.F. (1993). Contour integration by the human visual system: evidence for a local "association field". *Vision Research*, **33**, 173-193.

Fischl, B., Schwartz, E.L. (1997). Learning an integral equation approximation to nonlinear anisotropic diffusion in image processing. *IEEE Transactions on Pattern Analysis and Machine Intelligence*, **19**, 342-352.

Foster, K.H., Gaska, J.P., Nagler, M., & Pollen, D.A. (1985). Spatial and temporal frequency selectivity of neurones in visual cortical areas V1 and V2 of the macaque monkey. *Journal of Physiology*, **365**, 331-363.

Friedman, H.S., Zhou, H., & Von Der Heydt, R. (2003). The coding of uniform colour figures in monkey visual cortex. *Journal of Physiology*.

Fry, G.A. (1948). Mechanisms subserving simultaneous brightness contrast. *American Journal of Optometry and Archieves of the American Academy of Optometry*, **25**, 162-178.

Fry, G.A., & Alpern, M. (1953). The effect of a peripheral glare source upon the apparent brightness of an object. *Journal of the Optical Society of America*, **43**, 189-195.

Ghose, G.M., & Ts'o, D.Y. (1997). Form processing modules in primate area V4. *Journal Neurophysiology*, 77, 2191-2196.

Gilbert, C.D. (1977). Laminar differences in receptive field properties of cells in cat primary visual cortex. *Journal of Physiology (Lond)*, **268**, 391–421.

Gilbert, C.D., & Wiesel, T.N. (1979). Morphology and intracortical projections of functionally characterized neurones in the cat visual cortex. *Nature*, **280**, 120–125.

Gilchrist, A.L. (1977). Perceived lightness depends on perceived spatial arrangement. *Science*, **195**, 185-187.

Gilchrist, A.L. (1980). When does perceived lightness depend on perceived spatial arrangement? *Perception & Psychophysics*, **28**, 527-538.

Gilchrist, A.L., & Bonato, F. (1995). Anchoring of lightness values in center-surround displays. *Journal of Experimental Psychology - Human Perception and Performance*, **6**, 1427-1440.

Gilchrist, A.L., & Cataliotti, J. (1994). Anchoring of surface lightness with multiple illumination levels. *Investigative Ophthalmology and Visual Science*, **35**, S2165.

Gilchrist, A.L., Delman, S., & Jacobsen, A. (1983). The classification and integration of edges as critical to the perception of reflectance and illumination. *Perception & Psychophysics*, **33**, 425-436.

Gilchrist, A.L., Kossyfidis, C., Bonato, F., Agostini, T., Cataliotti, J., Li, X., Spehar, B., Annan, V., & Economou, E. (1999). An anchoring theory of lightness perception. *Psychological Review*, **106**, 795-834.

Gove, A., Grossberg, S., & Mingolla, E. (1995). Brightness perception, illusory contours, and corticogeniculate feedback. *Visual Neuroscience*, **12**, 1027-1052.

Grossberg, S. (1980). How does a brain build a cognitive code? *Psychological Review*, **87**, 1-51.

Grossberg, S. (1983). The quantized geometry of visual space: The coherent computation of depth, form and lightness. *Behavioral & Brain Sciences*, **6**, 625-692.

Grossberg, S. (1994). 3-D vision and figure-ground separation by visual cortex. *Perception & Psychophysics*, **55**, 48-120.

Grossberg, S. (1999). How does the cerebral cortex work? Learning, attention and grouping by the laminar circuits of visual cortex. *Spatial Vision, **12,** 163-186.*

Grossberg, S. (2000). The complementary brain: unifying brain dynamics and modularity. *Trends in Cognitive Sciences*, **4**, 233-246.

Grossberg S. (2003). Filling-in the forms: Surface and boundary interactions in visual cortex. In *Filling-in: From Perceptual Completion to Skill Learning* (eds., Pessoa, L & De Weerd P.). New York: Oxford University Press.

Grossberg S., & Howe, P.D.L. (2003). A laminar cortical model of stereopsis and three-dimensional surface perception. *Vision Research*, **43**, 801-829.

Grossberg, S., Hwang, S., & Mingolla, E. (2002). Thalamocortical dynamics of the McCollough effect: boundary-surface alignment through perceptual learning. *Vision Research*, **42**, 1259-1286.

Grossberg, S., & Kelly, F. (1999). Neural dynamics of binocular brightness perception. *Vision Research*, **39**, 3796-3816.

Grossberg, S. & McLoughlin, N. (1997). Cortical dynamics of 3-D surface perception: Binocular and half-occluded scenic images. *Neural Networks*, **10**, 1583-1605.

Grossberg, S., & Mingolla, E. (1985a). Neural dynamics of perceptual grouping: textures, boundaries, and emergent segmentations. *Perception & Psychophysics*. **38**, 141-71.

Grossberg, S., & Mingolla, E. (1985b). Neural dynamics of form perception: boundary completion, illusory figures, and neon color spreading. *Psychological Review*, **92**, 173-211.

Grossberg, S., Mingolla, E., & Williamson, J. (1995). Synthetic aperture radar processing by a multiple scale neural system for boundary and surface representation. *Neural Networks*, **7/8**, 1005-1028.

Grossberg, S., & Raizada, R.D. (2000). Contrast-sensitive perceptual grouping and object-based attention in the laminar circuits of primary visual cortex. *Vision Research*, **40**, 1413-1432.

Grossberg, S., & Swaminathan, G. (2004). A laminar cortical model for 3D perception of slanted and curved surfaces and of 2D images: development, attention and bistability. *Vision Research*, **44**, 1147-1187.

Grossberg, S., & Todorovic, D. (1988). Neural dynamics of 1-D and 2-D brightness perception: a unified model of classical and recent phenomena. *Perception & Psychophysics*, **43**, 241–277.

Grossberg, S., & Yazdanbakhsh, A. (2003). Laminar cortical dynamics of 3-D surface stratification, transparency, and neon spreading. *Journal of Vision*, *3*(9), 247a.

Grossberg, S., & Yazdanbakhsh, A. (2004). Laminar cortical dynamics of 3D surface perception: Stratification, transparency, and neon color spreading. Submitted.

Hahnloser, R.H., Douglas, R.J., & Hepp, K. (2002). Attentional recruitment of inter-areal recurrent networks for selective gain control. *Neural Computation*, **14**, 1669-1689.

Helmholtz, H. von, (1866). *Helmholtz's treatise on physiological optics*, New York: Optical Society of America.

Helson, H. (1943). Some factors and implications of color constancy. *Journal of the Optical Society of America*, **33**, 179-184.

Hering, E. (1920). Outline of a theory of the light sense, *trans. Hurvich, L. & Jameson, D. (1964)* (Harvard Univ. Press, Cambridge, MA).

Hong S, & Grossberg S (2003). Cortical Dynamics of Surface Lightness Anchoring, Filling-In, and Perception. *Vision Sciences Society, Third Annual Meeting, Sarasota, Florida*. pp. 120.

Hong S, & Grossberg S (2004). A neuromorphic model for achromatic and chromatic surface perception of natural images. *Neural Networks*, **17**, 787-808

Horn, B.K.P. (1977). Understanding image intensities. *Artificial Intelligence*, **21**, 201-231.

Huang, X., MacEvoy, S.P., & Paradiso, M.A. (2002). Perception of brightness and brightness illusions in the macaque monkey. *Journal of Neuroscience*, **22**, 9618-9625.

Hubel, D.H. & Wiesel, T.N. (1961). Integrative action in the cat's lateral geniculate body. *Journal of Physiology*, **155**, 385-398.

Hubel, D.H. & Wiesel, T.N. (1962). Receptive fields, binocular interaction and functional architecture in the cat's visual cortex. *Journal of Physiology (London)*, **160**, 106-154.

Hung, C.P., Ramsden, B.M., Chen, L.M., & Roe, A.W., (2001). Building surfaces from borders in Areas 17 and 18 of the cat. *Vision Research*, **41**, 1389-1407.

Hurlbert A. (1986). Formal connections between lightness algorithms. Journal of the Optical Society of America A. 3, 1684-1693.

Hurley, J.B. (2002). Shedding light on adaptation. *Journal of General Physiology*, **119**, 125-128.

Hupé, J.M., James, A.C., Payne, B.R., Lomber, S.G., Girard, P., & Bullier, J. (1998). Cortical feedback improves discrimination between figure and background by V1, V2 and V3 neurons. *Nature*, **394**, 784-787.

Hupé, J.M., James, A.C., Girard, P., & Bullier, J. (2001). Response modulations by static texture surround in area V1 of the macaque monkey do not depend on feedback connections from V2. *Journal of Neurophysiology*, **85**, 146-63.

Issa N.P., Trepel, C., & Stryker, M.P., (2000). Spatial frequency maps in cat visual cortex. *Journal of Neuroscience*, **20**, 8504-8514.

Jameson, D., & Hurvich, L.M. (1989). Essay concerning color constancy. *Annual Review of Psychology*, **40**, 1-22.

Jobson, D.J., Rahman, Z., & Woodell, G.A. (1997a). Properties and Performance of a Center/Surround Retinex. *IEEE Transactions on Image Processing*, March.

Jobson, D.J., Rahman, Z., & Woodell, G.A. (1997b). A Multi-Scale Retinex For Bridging the Gap Between Color Images and the Human Observation of Scenes. *IEEE Transactions on Image Processing: Special Issue on Color Processing*, July.

Jones, E.G., (1994). GABA neurons and their role in activity-dependent plasticity of adult primate visual cortex. In *Cerebral Cortex,* ed. A Peters, KS Rockland, **10**, 61-140. New York: Plenum.

Jones, H.E., Andolina, I.M., Oakely, N.M., Murphy, P.C., & Sillito, A.M. (2000). Spatial summation in lateral geniculate nucleus and visual cortex. *Experimental Brain Research*, **135**, 279-284.

Kaas, J.H., & Collins, C.E. (2001). The organization of sensory cortex. *Current Opinion in Neurobiology*, **11**, 498-504.

Kahrilas, P.J., Doty, R.W., & Bartlett, J.R. (1980). Failure to find luxotonic responses for single units in visual cortex of the rabbit. *Experimental Brain Research*, **39**, 11-16.

Kamermans, M., Haak, J., Habraken, JB., & Spekreijse, H. (1996). The size of the horizontal cell receptive fields adapts to the stimulus in the light adapted goldfish retina. *Vision Research*, **36**, 4105-4119.

Kamitani, Y., & Shimojo, S. (inpress). Global yet early processing of visual surfaces. In *The Visual Neurosciencies* (eds. Chalupa, L.M. & Werner, J.S.), MIT Press.

Kaufman, L. (1974). Sight and mind. New York, NY: Oxford University Presser

Kayama, Y., Riso, R.R., Bartlett, J.R., & Doty, R.W. (1979). Luxotonic responses of units in macaque striate cortex. *Journal of Neurophysiology*, **42**, 1495-1517.

Kellman, P.J., & Shipley, T.F. (1991). A theory of visual interpolation in object perception. *Cognitive Psychology*, **23**, 141-221.

Kelly, F., & Grossberg, S., (2000). Neural dynamics of 3-D surface perception: figure-ground separation and lightness perception. *Perception & Psychophysics*, **62**, 1596-1618.

Kimmel, R., Elad, M., Shaked, D., Keshet, R. & Sobel, I. (2002). A Variational Framework to Retinex. *The International Journal on Computer Vision*, July.

Kinoshita, M., & Komatsu, H. (2001). Neural representation of the luminance and brightness of a uniform surface in the macaque primary visual cortex. *Journal of Neurophysiology*, **86**, 2559-2570.

Kobatake, E., & Tanaka, K. (1994). Neuronal selectivities to complex object feature, in the ventral visual pathway of the macaque cerebral cortex. *Journal of Neurophysiology*, **71**, 856-867.

Kobayashi, M., Imamura, K., Sugai, T., Onoda, N., Yamamoto, M., Komai, S., & Watanabe, Y. (2000). Selective suppression of horizontal propagation in rat visual cortex by norepinephrine. *European Journal of Neuroscience*, **12**, 264-272.

Koutalos, Y., & Yau, K.W. (1996). Regulation of sensitivity in vertebrate rod photoreceptors by calcium. *Trends in Neuroscience*, **19** , 73-81.

Komatsu, H., Kinoshita, M., & Murakami, I. (2000). Neural Responses in the Retinotopic Representation of the Blind Spot in the Macaque V1 to Stimuli for Perceptual Filling-In. *Journal of Neuroscience*, **20**, 9310-9319.

Komatsu, H., Murakami, I., & Kinoshita, M. (1996). Surface representation in the visual system. *Cognitive Brain Research*, **5**, 97-104.

Kuffler, S.W. (1953). Discharge patterns and functional organization of mammalian retina. *Journal of Neurophysiology*, **16**, 37-68.

Lambert, J.H. (1760): Photometria sive de mensura et gradibus luminis, colorum et umbrae. Augsburg (German translation by E. Anding, Klett: Leipzig 1892).

Lamme, V.A., (2001). Blindsight: the role of feedforward and feedback corticocortical connections. *Acta Psychologica (Amsterdam)*, **107**, 209-228.

Lamme, V.A., Zipser, K., & Spekreijse, H. (1998). Figure-ground activity in primary visual cortex is suppressed by anesthesia. *Proc Natl Acad Sci* U S A, **95**, 3263-3268.

Land, E.H., & McCann, J.J. (1971). Lightness and Retinex theory, *Journal of the Optical Society of America*, **61**, 1-11.

Lee, A.B., Blais, B., Shouval, H.Z., & Cooper, L.N., (2000). Statistics of lateral geniculate nucleus (LGN) activity determine the segregation of ON/OFF subfields for simple cells in visual cortex. *Proc Natl Acad Sci U S A*, **97**, 12875-12879.

Lee, B.B., Dacey, D.M., Smith, V.C., & Pokorny, J. (1999). Horizontal cells reveal cone type-specific adaptation in primate retina. *Proc Natl Acad Sci U S A*, **96**, 14611-14616.

Legg, C.R., & Cowey, A. (1977a). Effects of subcortical lesions on visual intensity discriminations in rats. *Physiology & Behavior,* **19**, 635-646.

Legg, C.R., & Cowey, A. (1977b). The role of the ventral lateral geniculate nucleus and posterior thalamus in intensity discrimination in rats. *Brain Research*, **123**, 261-273.

Libowitz, H. Mote, F.A. & Thurlow, W.R. (1953). Simultaneous contrast as a function of separation between test and inducing fields. *Journal of Experimental Psychology*, **46**, 453-456.

Livingstone, M. S. & Hubel, D. H. (1981). Effects of sleep and arousal on the processing of visual information in the cat. *Nature*, **291**, 554-561

Lu, C., Zhang, D.Q., & McMahon, D.G. (1999). Electrical coupling of retinal horizontal cells mediated by distinct voltage-independent junctions. *Visual Neuroscience*, **16**, 811-818

MacEvoy, S.P., Kim, W., & Paradiso, M.A. (1998). Integration of surface information in primary visual cortex. *Nature Neuroscience*, **1**, 616-620.

MacEvoy, S.P., & Paradiso, M.A. (2001). Lightness constancy in primary visual cortex. *Proc Natl Acad Sci USA*, **98**, 8827-8831.

Marrocco, R.T. (1972). Maintained activity of monkey optic tract fibers and lateral geniculate nucleus cells. *Vision Research*, **12**, 1175-1181.

Martin, G.R. (1983). Schematic eye models in vertebrates. *Progress in Sensory Physiology*, **4**, 44–81.

Martinez, L.M., & Alonso, J.M. (2001). Construction of complex receptive fields in cat primary visual cortex. *Neuron*, **32**, 515-525.

Masland, R.H. (2001). The fundamental plan of the retina. *Nature Neuroscience*, **4**, 877-886.

McMahon, D.G. (1994). Modulation of electrical synaptic transmission in zebrafish retinal horizontal cells. *Journal of Neuroscience*. **14**, 1722-1734

McMahon, D.G., Zhang, D.Q., Ponomareva, L., & Wagner, T. (2001). Synaptic mechanisms of network adaptation in horizontal cells. *Progress in Brain Research*, **131**, 419-436

Mechler, F., & Ringach, D.L. (2002). On the classification of simple and complex cells. *Vision Research*, **42**, 1017-1033.

Meister, M., & Berry, M.J. 2nd (1999). The neural code of the retina. *Neuron*, **22**, 435-450.

Mills, S.L., & Massey, S.C. (1995). Differential properties of two gap junctional pathways made by AII amacrine cells. *Nature*, **377**, 734-737.

Mingolla, E., Ross, W., & Grossberg, S., (1999). A neural network for enhancing boundaries and surfaces in synthetic aperture radar images. *Neural Networks*, **12**, 499-511.

Moore, R.Y., Weis, R., & Moga, M.M. (2000). Efferent projections of the intergeniculate leaflet and the ventral lateral geniculate nucleus in the rat. *Journal of Comparative Neurology,* **420**, 398-418.

Naka, K.I., & Rushton, W.A. (1967). The generation and spread of S-potentials in fish (Cyprinidae). *Journal of Physiology*, **192**, 437-461.

Nakamura, H., Gattass, R., Desimone, R., & Ungerleider, L.G. (1993). The modular organization of projections from areas V1 and V2 to areas V4 and TEO in macaques. *Journal of Neuroscience*, **13**, 3681-3691.

Nakatani, K., Tamura, T., & Yau, K.W. (1991). Light adaptation in retinal rods of the rabbit and two other nonprimate mammals. *Journal of General Physiology*, **97**, 413–435.

Nakayama, K., & Shimojo, S. (1992). Experiencing and perceiving visual surfaces. *Science*, **257**, 1357-1363.

Nawy, S. (2000). Regulation of the on bipolar cell mGluR6 pathway by Ca^{2+}. *Journal of Neuroscience*, **20**, 4471-4479.

Neumann, H., Pessoa, L., & Mingolla, E. (1998). A neural architecture of brightness perception: non-linear contrast detection and geometry-driven diffusion. *Image and Vision Computing*, **16**, 423-446.

Neumann, H., Pessoa, L., & Hansen, T. (2001). Visual filling-in for computing perceptual surface properties. *Biological Cybernetics*, **85**, 355-369.

Neumann, H., & Sepp, W. (1999). Recurrent V1–V2 interaction in early visual boundary processing. *Biological Cybernetics,* **81**, 425–444.

Newson, L.J. (1958). Some principles governing changes in the apparent lightness of test surfaces isolated from their normal backgrounds. *Quarterly Journal of Experimental Psychology*, **10**, 82-95.

Papaioannou, J., & White, A. (1972). Maintained activity of lateral geniculate ucleus neurons as a function of background luminance. *Experimental Neurology*, **34**, 558-566.

Paradiso, M.A., & Nakayama, K. (1991). Brightness perception and filling-in. *Vision Research*, **31**, 1221-1236.

Pessoa, L., Mingolla, E., & Arend, L.E. (1996). The perception of lightness in 3-D curved objects. *Perception & Psychophysics*, **58**, 1293-1305.

Pessoa, L., Mingolla, E., & Neumann, H. (1995). A contrast- and luminance-driven multiscale network model of brightness perception. *Vision Research*, **35**, 2201-2223.

Pessoa, L., & Neumann, H. (1998). Why does the brain fill-in? *Trends in Cognitive Sciences*, **11**, 422-424.

Peterhans, E., von der Heydt, R. (1989). Mechanisms of contour perception in monkey visual cortex. II. Contours bridging gaps. *Journal of Neuroscience*, **9**, 1749-1763.

Pinna, B., Brelstaff, G., & Spillmann, L. (2001). Surface color from boundaries: a new 'watercolor' illusion. *Vision Research*, **41**, 2669-2676.

Pinna, B., Werner, J.S., & Spillmann, L. (2003). The watercolor effect: a new principle of grouping and figure-ground organization. *Vision Research*, **43**, 43-53.

Posner, M.I., Snyder, C.R.R. & Davidson, B.J. (1980). Attention and the detection of signals. *Journal of Experimental Psychology*, **109**, 160-174

Przybyszewski, A.W., Gaska, J.P., Foote, W., & Pollen, D.A. (2000). Striate cortex increases contrast gain of macaque LGN neurons. *Visulal Neuroscience*, **17**, 485-494.

Rahman, Z., Jobson, D. J., & Woodell, G. A. (1996). Multiscale retinex for color image enhancement. *International Conference on Image Processing (ICIP)'96*.

Rahman, Z., Woodell, G. A., & Jobson, D. J (1997). A comparison of the multiscale retinex with other image enhancement techniques. *Proceedings of the IS and T 50th Anniversary Conference*.

Raizada, R.D.S. & Grossberg, S. (2001). Context-sensitive binding by the laminar circuits of V1 and V2: A unified model of perceptual grouping, attention, and orientation contrast. *Visual Cognition*, **8**, 431-466.

Raizada, R.D.S. & Grossberg, S. (2003). Towards a theory of the laminar architecture of cerebral cortex: computational clues from the visual system. *Cerebral Cortex*, **13**, 100-113.

Reid, R.C., & Alonso, J.M. (1995). Specificity of monosynaptic connections from thalamus to visual cortex. *Nature*, **378**, 281-284.

Reynolds, J.H., Chelazzi, L., & Desimone, R. (1999). Competitive mechanisms subserve attention in macaque areas V2 and V4. *Journal of Neuroscience*, **19**, 1736-1753.

Ribelayga, C., Wang, Y., & Mangel, S.C. (2002). Dopamine mediates circadian clock regulation of rod and cone input to fish retinal horizontal cells. *Journal of Physiology*, **544**, 801-816.

Ringach, D.L. (2002). Spatial structure and symmetry of simple-cell receptive fields in macaque primary visual cortex. *Journal of Neurophysiology,* **88**, 455-463.

Rockland, K.S., & Lund, J.S. (1982). Widespread periodic intrinsic connections in the tree shrew visual cortex. *Science*, **215**, 1532–1534.

Rodieck, R.W. (1998). The first steps in seeing. Sunderland, MA: Sinauer.

Rodieck, R.W. (1965). Quantitative analysis of cat retinal ganglion cell response to visual stimuli. *Vision Research*, **5**, 583–601.

Rodieck, R.W., & Stone, J. (1965). Response of cat retinal ganglion cells to moving visual patterns. *Journal of Neurophysiology*, **28**, 819–832.

Roe, A.W., & Ts'o, D.Y. (1995). Visual topography in primate V2: multiple representation across functional stripes. *Journal of Neuroscience*, **15**, 3689-3715.

Roe, A.W. & Ts'o, D.Y., (1999). Specificity of color connectivity between primate V1 and V2. *Journal of Neurophysiology*, **82**, 2719–2730.

Roska, B., Nemeth, E., Orzo, L. & Werblin, F.S. (2000). Three levels of lateral inhibition: a space-time study of the retina of the tiger salamander. *Journal of Neuroscience*, **20**, 1941-1951.

Roska, B., & Werblin, F.S. (2001). Vertical interactions across ten parallel, stacked representations in the mammalian retina. *Nature*, **410**, 583-587.

((Ross, W.D., & Pessoa, L. (2000). Lightness from contrast: a selective integration model. *Perception & Psychophysics*, **62**, 1160-1181.))

Rossi, A.F., & Paradiso, M.A. (1999). Neural correlates of perceived brightness in the retina, lateral geniculate nucleus, and striate cortex. *Journal of Neuroscience*, **19**, 6145-6156

Rossi, A.F., Rittenhouse, C.D., & Paradiso, M.A. (1996). The representation of brightness in primary visual cortex. *Science*, **273**, 1104-1107.

Rozas, C., Frank, H., Heynen, A.J., Morales, B., Bear, M.F., & Kirkwood, A. (2001). Developmental inhibitory gate controls the relay of activity to the superficial layers of the visual cortex. *Journal of Neuroscience*, **21**, 6791-6801.

Ruksenas, O., Fjeld, I.T. & Heggellund, P. (2000). Spatial summation and center-surround antagonism in the receptive field of single units in the dorsal lateral geniculate nucleus of cat: Comparison with retinal input. *Visual Neuroscience*, **17**, 855 –870.

Sakai, K., & Tanaka, S. (2000). Spatial pooling in the second-order spatial structure of cortical complex cells. *Vision Research*, **40**, 855-871.

Sasaki, Y., Watanabe, T., Dale, A.M., & Tootell, R.B. (2001). V1 involvement for color filling-in revealed by human fMRI. *Society for Neuroscience Abstract*s:12.11.

Schiller, P.H. (1992). The ON and OFF channels of the visual system. *Trends in Neuroscience*, **15**, 86-92.

Schiller, P.H., Finlay, B.L., & Volman, S.F. (1976). Quantitative studies of single-cell properties in monkey striate cortex. V. Multivariate statistical analyses and models. *Journal of Neurophysiology*, **39**, 1362-1374.

Schiller, P.H., Sandell, J.H., & Maunsell, J.H. (1986). Functions of the ON and OFF channels of the visual system. *Nature*, **322**, 824-825.

Schirillo, J., Reeves, A., & Arend, L. (1990). Perceived lightness, but not brightness, of achromatic surfaces depends on perceived depth information. *Perception & Psychophysics*, **48**, 82-90.

Schwartz, E. (1980). Computational anatomy and functional architecture of striate cortex: a spatial mapping approach to perceptual coding. *Vision Research*, ***20***, 645–699.

Sepp, W., & Neumann, H., (1999). A multi-resolution filling-in model for brightness perception, *Ninth International Conference on Artificial Neural Networks*. **1**, 461-466.

Shapley, R., & Enroth-Cugell, C. (1984). Visual adaptation and retinal gain controls. *Progress in Retinal Research*, **3**, 263–346.

Sherman, S.M. (1996). Dual response modes in lateral geniculate neurons: mechanisms and functions. *Visual Neuroscience*, **13**, 205–213.

Sherman, S.M. (2001). Tonic and burst firing: dual modes of thalamocortical relay. *Trends in Neuroscience*, **24**, 122-126.

Shevelev, I.A. (1998). Second-order feature extraction in the cat visual cortex: selective and invariant sensitivity of neurons to the shape and orientation of crosses and corners. *Biosystems*, **48**, 195-204.

Shevelev, I.A. (2000). Sensitivity of striate neurons to Y-like figures: experiment and simulation. *Biosystems*, **58**, 211-217.

Shevelev, I.A., Lazareva, N.A., Sharaev, G.A., Novikova, R.V., & Tikhomirov, A.S. (1998). Selective and invariant sensitivity to crosses and corners in cat striate neurons. *Neuroscience*, **84**, 713-721.

Sillito, A.M., Jones, H.E., & Gerstein, G.L. (1994). West DC, Feature-linked synchronization of thalamic relay cell firing induced by feedback from the visual cortex. *Nature*, **369**, 479-482.

Sillito, A.M., Kemp, J.A. & Beradi, N. (1983). The cholinergic influence on the function of the cat dorsal lateral geniculate nucleus (dLGN). *Brain Research*, **280**, 299 –307.

Smirnakis, S.M., Berry, M.J., Warland, D.K., Bialek, W., & Meister, M. (1997). Adaptation of retinal processing to image contrast and spatial scale. *Nature,* **386**, 69-73.

Solomon, S.G., White, A.J., Martin, P.R. (2002). Extraclassical receptive field properties of parvocellular, magnocellular, and koniocellular cells in the primate lateral geniculate nucleus. *Journal of Neuroscience*, **22**, 338-349.

Somers, D.C., Dale, A.M., Seiffert, A.E., & Tootell, R.B. (1999). Functional MRI reveals spatially specific attentional modulation in human primary visual cortex. *Proc Natl Acad Sci USA*, **96**, 1663-1668.

Somers, D.C., Todorov, E.V., Siapas, A.G., Toth, L.J., Kim, D.S., & Sur, M., (1998). A local circuit approach to understanding integration of long-range inputs in primary visual cortex. *Cerebral Cortex*, **8**, 204-217.

Spillmann, L. (1994). The Hermann Grid Illusion: a Tool for Studying Human Perceptive Field Organization. *Perception*, **23**, 691-708.

Spray, D.C., Harris A.L., & Bennett M.V. (1979). Voltage dependence of junctional conductance in early amphibian embryos. *Science*, **204**, 432-434.

Stanley, G.B., Li, F.F., & Dan, Y. (1999). Reconstruction of natural scenes from ensemble responses in the lateral geniculate nucleus. *Journal of Neuroscience*, **19**, 8036-8042.

Sterling, P. in *The Synaptic Organization of the Brain* Vol. 4 (ed. Shepherd, G. M.), 205-253 (Oxford Univ. Press, New York, 1998).

Stettler, D.D., Das, A., Bennett, J., & Gilbert, C.D. (2002). Lateral connectivity and contextual interactions in macaque primary visual cortex. *Neuron*, **36**, 739-750.

Suder, K., Wörgötter, F., & Wennekers, T. (2001). Neural field model of receptive field restructuring in primary visual cortex. *Neural Computation*, **13**, 139-159.

Tadmor, Y., & Tolhurst, D.J. (2000). Calculating the contrasts that retinal ganglion cells and LGN neurons encounter in natural scenes. *Vision Research*, **40**, 3145-3157.

Thibos, L.N., & Werblin, F.S. (1978). The response properties of the steady antagonistic surround in the mudpuppy retina. *Journal of Physiology*, **278**, 79-99.

Todorović, D. (1997). Lightness and junctions. *Perception*, **26**, 379-394.

Tomita, T. (1965). Electrophysiological study of the mechanisms subserving color coding in the fish retina. *Cold Spring Harbor Symposium on Quantitative Biology*, **30**, 559-66.

Triesman, A.M. & Sato, S. (1990). Conjunction search revisited. *Journal Of Experimental Psychology-Human Perception And Performance*, **16**, 459-478

Troyer, T.W., Krukowski, A.E., Priebe, N.J., & Miller, K.D. (1998). Contrast-invariant orientation tuning in cat visual cortex: thalamocortical input tuning and correlation-based intracortical connectivity. *Journal of Neuroscience*, **18**, 5908-5927.

Ts'o, D.Y., Roe, A.W., & Gilbert, C.D. (2001). A hierarchy of the functional organization for color, form and disparity in primate visual area V2. *Vision Research*, **41**, 1333-1349.

Usrey, W.M., Sceniak, M.P., & Chapman, B. (2003). Receptive fields and response properties of neurons in layer 4 of ferret visual cortex. *Journal of Neurophysiology*, **89**, 1003-1015.

Verweij, J., Kamermans, M., & Spekreijse, H. (1996). Horizontal cells feed back to cones by shifting the cone calcium-current activation range. *Vision Research*, **36**, 3943-3953.

von der Heydt, R., Peterhans, E., & Baumgartner, G. (1984). Illusory contours and cortical neuron responses. *Science*, **224**, 1260-1262.

Wallach, H. (1948). Brightness constancy and the nature of achromatic colors. *Journal of Experimental Psychology*, **38**, 310-324.

Wallach, H. (1976). *On perception*, New York: Quadrangle/The New Your Times Book Co.

Welchman, A.E., & Harris, J.M. (2001). Filling-in the details on perceptual fading. *Vision Research*, **41**, 2107-2117.

Werblin, F.S. (1971). Adaptation in a vertebrate retina: intracellular recording in Necturus. *Journal of Neurophysiology*, **34**, 228-241.

Werblin, F.S. (1974). Control of retinal sensitivity. II. Lateral interactions at the outer plexi form layer. *Journal of General Physiology*, **63**, 62-87.

Werblin, F.S., & Dowling, J.E. (1969). Organization of the retina of the mudpuppy. *Necturus maculosus*. II. Intracellular recording. *Journal of Neurophysiology*, **32**, 339-355.

Werblin, F.S., Roska, B., & Balya, D. (2001). Parallel processing in the mammalian retina: lateral and vertical interactions across stacked representations. *Progress in Brain Research*, **131**, 229-238.

Witkovsky, P. & Dearry A. (1991). Functional roles of dopamine in the vertebrate retina. *Progress in Retinal Research*, **11**, 247–292.

Wörgötter, F., Suder, K., Zhao, Y., Kerscher, N., Eysel, U.T., & Funke, K. (1998). State-dependent receptive-field restructuring in the visual cortex. *Nature*, **396**, 165-8.

Wyszecki, G., & Stiles, W. S. (1982). *Color Science : Concepts and Methods, Quantitative Data and Formulae* (2nd ed.). New York: John Wiley & Sons.

Xin, D., & Bloomfield, S.A. (1999). Dark- and light-induced changes in coupling between horizontal cells in mammalian retina. *Journal of Comparative Neurology*, **405**, 75-87.

Xin, D., & Bloomfield, S.A. (2000). Effects of nitric oxide on horizontal cells in the rabbit retina. *Visual Neuroscience*. **17**, 799-811.

Yarbus, A.L. (1967). *Eye movements and vision*. Plenum Press.

Yabuta, N.H., & Callaway, E.M. (1998). Cytochrome-oxidase blobs and intrinsic horizontal connections of layer 2/3 pyramidal neurons in primate V1. *Visual Neuroscience*. **15**, 1007-1027.

Zhou, H., Friedman, H.S., & von der Heydt, R. (2000). Coding of border ownership in monkey visual cortex. *Journal of Neuroscience*, **20**, 6594-6611.

Zipser, K., Lamme, V.A., & Schiller, P.H. (1996). Contextual modulation in primary visual cortex. *Journal of Neuroscience*, **16**, 7376-7389.